Journal Pre-proofs

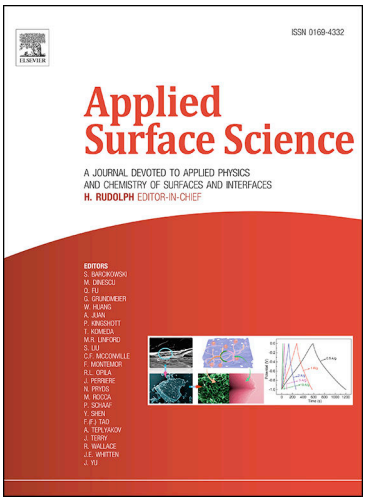

Full Length Article

Connecting the surface structure, morphology and photocatalytic activity of Ag_2O: An in depth and unified theoretical investigation

R.A.P. Ribeiro, Marisa C. Oliveira, Maurício R.D. Bomio, S.R. de Lazaro, J. Andrés, E. Longo

PII: S0169-4332(20)30077-5
DOI: https://doi.org/10.1016/j.apsusc.2020.145321
Reference: APSUSC 145321

To appear in: *Applied Surface Science*

Received Date: 23 October 2019
Revised Date: 11 December 2019
Accepted Date: 7 January 2020

Please cite this article as: R.A.P. Ribeiro, M.C. Oliveira, M.R.D. Bomio, S.R. de Lazaro, J. Andrés, E. Longo, Connecting the surface structure, morphology and photocatalytic activity of Ag_2O: An in depth and unified theoretical investigation, *Applied Surface Science* (2020), doi: https://doi.org/10.1016/j.apsusc.2020.145321

Connecting the surface structure, morphology and photocatalytic activity of Ag_2O: An in depth and unified theoretical investigation

R. A. P. Ribeiro[1,*], Marisa C. Oliveira,[2] Maurício R. D. Bomio,[2] S. R. de Lazaro,[3] J. Andrés[4*], E. Longo[1*]

[1] *CDMF-UFSCar, Universidade Federal de São Carlos, PO Box 676, 13565–905 São Carlos, SP, Brazil*

[2] *LSQM- Laboratório de Síntese Química de Materiais, DEMat, Universidade Federal do Rio Grande do Norte - UFRN, P.O. Box 1524, 59078-970 Natal, RN, Brazil*

[3] *Department of Chemistry, State University of Ponta Grossa, Av. General Carlos Cavalcanti, 4748, 84030-900, Ponta Grossa, PR, Brazil*

[4] *Department of Physical and Analytical Chemistry, University Jaume I (UJI), Castelló 12071, Spain*

**corresponding authors; Email address: ribeiroapr@gmail.com; elson.liec@gmail.com; andres@qfa.uji.es*

ABSTRACT

The surface morphology of the materials is known to have significant influence on the overall photocatalytic performance. Therefore, identifying the corresponding electronic structures associated with the surface redox centers is essential for the rational design of Ag_2O-based photocatalysts. In this study, comprehensive and systematic theoretical calculations revealed the connection between electronic structure and morphology responsible for the photo-induced mechanism. First-principles calculations showed that the activity of Ag^+ cations on the exposed surfaces is dependent of their local coordination and electronic configuration. Electrons were found to migrate to the energetically favorable (111) surface, while holes are concentrated in the more unstable (100) and (110) surfaces. The complete set of available morphologies was obtained, enabling us to rationalize the photocatalytic activity in terms of composition, geometry, and electronic structure of the exposed surfaces. Moreover, the localization and characterization of excited electronic states of both bulk material and exposed surfaces allow us to discuss the fundamental reactions involved in the photocatalytic mechanism underlying the morphological evolution and would promote significantly the development and application of singlet-triplet mechanism. The detailed insights provided by our work could benefit the design and preparation of new efficient photocatalysts based on Ag_2O.

Keywords: Photocatalysis, Ag_2O, surface structure, density functional theory, morphology, fundamental and excited electronic states.

1. Introduction

The environmental theme certainly has been extremely discussed in the world. Climate change is one of most subject of intense investigation and discussion because of the point of views economic, social and political narrowing the perception on our influence in the sensitive climate equilibrium of the world. In the past few years, the field of photocatalysis has gained considerable importance in environmental technologies, due to the possibility of using solar irradiation to activate chemical processes, destroy undesired compounds, or generate chemical energy, such as in hydrogen production from H_2O.[1-2]Heterogeneous photocatalysis has proved its efficiency for the degradation of chemical contaminants through photo-induced reactions in presence of a semiconductor photocatalyst. This method originated in the 1970s, when Fujishima and Honda reported water splitting by a photoelectrochemical cell containing TiO_2.[3] Subsequently, the scientific and technological interest in such methods has exponentially increased, makingTiO_2 the widely used semiconductor material for the generation of charge carriers. However, due to its large band-gap (3.2 eV), anatase TiO_2 only absorbs UV light, which accounts for 4–5% of the solar spectrum; therefore, extensive studies are required to identify more suitable visible light-sensitive photocatalysts.[4-5]

A precise understanding of the morphology of semiconductor materials is critical to identify the correlations between crystalline structure, activity, and technological applications; the latter can be improved and stabilized by tailoring the surface structures and exposed crystal faces of the material.[6-12] The preparation of semiconductor oxides crystals with tunable morphologies is based on the control of the exposed surfaces. It is well known that the strong dependence of the surface energy (E_{surf}) on the surface orientation can be understood from the viewpoint of different distributions of the surface atoms on the exposed surfaces appearing at the morphology, as atomic distribution strongly influences the surface electronic structure. In this context, semiconductors can vary from highly conductive to nonconductive, and can be highly photocatalytically active or inactive depending upon the different electronic structure of the different surfaces.[13-14] In fact, several studies have been devoted to explain the wide connection between morphology, electronic structure, and photocatalytic properties, and the rational design of facet-dependent synthesis has emerged as an excellent tool to select surfaces with superior activities for much kind of materials.[10, 15-17]

Silver oxide (Ag_2O) has proved its efficiency in a wide range of technological applications such as photocatalysis, bactericides, colorants, and electrode materials.[18-21] In particular, experimental evidences highlighted the strong dependence of its photocatalytic activity on the presence of exposed (100), (110), and (111) surfaces. In this context, facet-dependent photocatalytic processes are associated with the shape and size of Ag_2O particles, and the cubic, octahedral, rhombic dodecahedral, and rhombicuboctahedral morphologies appear favorable to obtain superior activities.[13-14, 20, 22-24] In addition, the importance of oxygen vacancies for manipulating the electronic properties of metal oxides is well established in water splitting applications;[25-26]in particular, structural and electronic disorder, primarily in the form of oxygen vacancies, cation stoichiometry, and atomic diffusion processes play a major effect on the electronic properties of Ag_2O.[27-31]

From a theoretical point of view, some studies aimed to understand the photocatalytic properties of Ag_2O focusing on the electronic structure of the semiconductor.[32-36] Umezawa *et al*. compared the photocatalytic performance of Ag_3PO_4 and Ag_2O and reported that carrier separation is effective on Ag_2O (100) and (110) surfaces.[36] In other studies, the electronic structure of several Ag-based oxides were compared focusing on the band-gap region and the orbitals associated with the photo-induced processes.[32-33] However, the relation between crystal morphology, electronic structure, and photocatalytic properties remains unclear.

Based on the above considerations, in this study, we present a theoretical investigation of the energetic, structural, and electronic properties of Ag_2O bulk and its surfaces, aiming to not only rationalize the experimental results, but also determine the nature of the photo-induced carriers and the shape-dependent photocatalytic mechanism. The main novelty of this work lies in the identified correlation of the morphology and electronic structure of both bulk material and exposed surfaces (appearing in the morphology) with the photocatalytic activity. The purpose of this work is twofold. First, we aim to provide insight on the geometrical and electronic nature of Ag_2O bulk based on explicit and realistic models. The second goal is to rationalize the experimental results and understand the origin of the photoactivity by identifying the nature of the photo-induced carriers and the shape-dependent photocatalytic mechanism. We provide robust

theoretical evidences that such dependence is intrinsically associated with the separation of the photo-generated charge carriers.

This paper contains three more sections. The next section is devoted to the computational methods and model systems. In section three, the results are presented and discussed. The main conclusions are summarized in the fourth and final section.

2. Computational Methods and Model Systems

In this study, density functional theory (DFT) calculations were performed within the linear combination of atomic orbitals approach, as implemented in the CRYSTAL14 code.[37] Ag and O atoms were described by the HAYWSC-311d31G effective core pseudopotential and by the atom-centered all-electron 8-411G Gaussian basis set, respectively. In all calculations, the B3LYP[38] hybrid functional was employed for the treatment of exchange and correlation effects. The analyses of the electronic properties in terms of Density of States (DOS) projections, band structure profiles, and electronic density distributions were carried out with the new property evaluation functionalities available in the latest version of the CRYSTAL code.[39]

The pristine cubic (*Pn*-3*m*) unit cell is modeled by two Ag_2O unit formulas (six atoms), with Ag and O atoms located at (0; 0; 0) and (0.25; 0.25; 0.25), respectively. Neutral (V_O^x and V_{Ag}^x) and charged ($V_O^{\bullet}$, $V_O^{\bullet\bullet}$and V'_{Ag}) vacancies were modeled by embedding them in 2×2×2 Ag_2O supercells containing 48 atoms, as shown in Figure 1. In this study, the Kröger–Vink[40] notation was implemented to represent the neutral and charged defects, where symbols [X^x], [$X^{\bullet}$] and [X'] correspond to the neutral, positive charged and negative charged defects, respectively.

Figure 1

Electronic integration was performed using a 4×4×4 Monkhorst-Pack[41] *k*-mesh for the pristine and defective cells, containing 10*k*-points. The accuracy of the Coulomb and exchange integral calculations were controlled by five thresholds set to 8, 8, 8, 8, and 16. The converge criterion for mono- and bi-electronic integrals were set to 10^{-8} Ha, while the root-mean-square (RMS) gradient, RMS displacement, maximum gradient, and maximum displacement were set to 3 $\times10^{-4}$, 1.2 $\times10^{-3}$, 4.5 $\times10^{-4}$, and 1.8 $\times10^{-3}$ a.u.,

respectively. Lattice parameters and atomic positions were fully relaxed for both pristine and defective models.

As it was previously mentioned, the values of the E_{surf} for the different exposed surfaces of a crystal are the key parameters that control their morphology and may affect the photocatalytic performance that should be rationally selected. In order to evaluate the physical and chemical properties associated with Ag_2O surfaces, a slab model was employed. In particular, the chemical structure of each surface was described as a two-dimensional periodic film formed by atomic layers parallel to the (*hkl*) crystalline plane of interest, cut from the optimized bulk geometry of the selected (100), (110), and (111) surfaces. In this context, we ascertain that (110) and (100) surfaces are polar, i. e. containing two slab terminations, which cannot be made equivalent. Then, we have used a theoretical procedure to obtain the values of E_{surf} without surface reconstructions, chemical adsorptions or polarity compensation mechanism.[42-43] In this context, Tian et al.[44] confirmed that asymmetric and stoichiometric slabs are the most suitable choice to take into account the calculation of cleavage energy for complementary Z^+/Z^- terminations and its relaxations, arguing that the reported method here for the calculation of E_{surf} could be extended to other similar systems with asymmetric surface terminations.[45] In the present study, E_{surf} was assumed to correspond for surface cleavage (E_{cleav}). Therefore, firstly, we introduce the concept of unrelaxed E_{cleav} as the required energy to cut the bulk along the selected plane.

$$\boldsymbol{E_{cleav}^{unrlx}} = \frac{(\boldsymbol{E_{slab}^{unrlx}} - \boldsymbol{nE_{bulk}})}{\boldsymbol{2A}} \quad (1)$$

Here, E_{slab}^{unrlx} *and* E_{bulk} correspond to the total energies for the unrelaxed slab model and the bulk unit (Z = 2) corrected by Zero-Point Energy, respectively, whereas n and A represent the number of bulk units used in the slab construction and the surface area, respectively. For polar surfaces, a relaxation process of both Z^+ and Z^- terminations is performed; then the $E_{relax}(Z^+|Z^-)$ is calculated as the difference between the total energies for relaxed and unrelaxed slabs, as follows:

$$\boldsymbol{E_{relax}(Z^+|Z^-)} = \frac{(\boldsymbol{E_{slab}^{unrlx}} - \boldsymbol{E_{slab}^{relax}})}{\boldsymbol{2A}} \quad \textbf{(2)}$$

Therefore, we assume that the E_{surf} can be write as the mean value for both terminations:

$$\boldsymbol{E_{surf}} = \boldsymbol{E_{cleav}^{relax}(Z^+|Z^-)} = \boldsymbol{E_{cleav}^{unrlx}} - \boldsymbol{E_{relax}(Z^+|Z^-)} \quad \textbf{(3)}$$

The convergence of the E_{surf} values with the slab thickness was tested for all surfaces. After the corresponding optimization process and thickness convergence tests, the repeat units were expressed as number of layers in the slab subtracted from thickness. Thus, the surfaces terminations were selected as O-Ag_2 [12 layers – 13.4 Å] for (100), Ag_2-O_2-Ag_2- [10 layers – 15.4 Å] for (110), and O-Ag_4-O [15 layers – 13.6 Å] for (111), giving rise to a minimal dipole moment. These numbers of layers were found sufficient to reach convergence. No constraints were placed on the atoms during geometry optimization for the outer Ag_2O layers, except for the conservation of the original crystal symmetry and for the slab central layers which were clamped to reproduce the bulk. We have showed the feasibility of our approach in Support Information. This procedure has allowed us[43, 46-50] to obtain the complete set of morphologies, based on the Wulff construction and the $E_{surf.}$

In order to analyze the relation between E_{surf} and the geometric characteristics of the exposed surfaces, the dangling bond density (D_b) was calculated from the number of broken bonds created per unit cell (N_b) on a particular surface of area A, according to the expression:[47]

$$\boldsymbol{D_b = \frac{N_b}{A}} \quad (4)$$

Based on the calculated values of E_{surf} for the three low-index crystals facets of Ag_2O is possible to determine the equilibrium shape and ideal morphology using the Wulff construction. Furthermore, by changing the relative values of E_{surf} of each surface, we obtained a map of the available morphologies for Ag_2O, as well as the pathways connecting the different morphologies, including octahedral, truncated octahedral, cubic, truncated cubic, rhombic dodecahedral, and rhombicuboctahedral ones. For this purpose, the polyhedron energy E_{pol} was calculated by summing the contributions of each surface plane to the morphology ($c_{[hkl]}$) and the corresponding $E_{surf}^{[hkl]}$ values (see Supporting Information), as follows:[10, 49]

$$\boldsymbol{E_{pol} = \sum c_{[hkl]} \cdot E_{surf}^{[hkl]}} \quad (5)$$

where $c_{[hkl]}$ is the percent contribution of the surface area to the total surface area of the polyhedron, and $E_{surf}^{[hkl]}$ is the surface energy of the corresponding surface. The energy profiles were calculated by decreasing or increasing the E_{surf} value of a given surface of the polyhedron.

During a typical photocatalytic process, charge generation under semiconductor photoexcitation takes place; thus it is imperative to characterize the corresponding excited electronic states that largely determines the overall performance of a photocatalyst. Both singlet (s*) and triplet (t*) excited states of Ag_2O were localized and characterized for both bulk and surface models, following the approach previously developed by our group.[48, 51-52] For s* model, we considered an off-center Ag displacement of 0.1 Å in the *z*-direction. In the present case, the t* state was modeled by fixing the difference between the spin-up (α) and spin-down (β) electron densities ($n\alpha - n\beta = 2$) during the self-consistent field calculations. Each excited state minimum was confirmed by checking that all vibrational modes had positive frequencies. DFT calculations using the B3LYP functional tend to overestimate the values of the vibrational frequencies; therefore, a scaling factor of 0.96 was used.[53]

3. Results and Discussion

3.1. Crystalline and Electronic Structure

The calculated structural parameters (lattice constants, unit cell volume, and bond distances) of Ag_2O are summarized in Table 1. In the cubic symmetry model of the Ag_2O, the lattice is composed by Ag^+ cations in a linear (180°) arrangement with two oxygen atoms and each oxygen anion is surrounded by four Ag^+ cations (O_{4c}) in a tetrahedral polyhedron. This structure is in reasonable agreement with previous experimental results[54] and theoretical calculations performed with HSE06 hybrid functional.[32]

Table 1. Experimental and theoretical lattice parameters, unit cell volume and bond lengths for Ag_2O. The lattice parameters for all defective models were fixed as the optimized values obtained for pristine Ag_2O.

	a = b = c (Å)	V (Å³)	Ag-O (Å)	Ag-Ag (Å)
Ag_2O	4.849	114.01	2.100 (2x)	3.429
Ag_2O: V_{Ag}^{x}	-	-	2.092 (2x)	3.387
Ag_2O: V'_{Ag}	-	-	2.077 (2x)	3.432
Ag_2O: V_{O}^{x}	-	-	2.223 (2x)	2.845
Ag_2O: $V_{O}^{\bullet}$	-	-	2.213 (2x)	2.901
Ag_2O: $V_{O}^{\bullet\bullet}$	-	-	2.202 (2x)	2.965
Experimental[a]	4.731	105.86	2.048 (2x)	3.345
Theoretical[b]	4.824	112.27	2.089 (2x)	3.544

[a] Ref. [54] [b] Ref. [32]

Compared with the model of the pristine material, the creation of the neutral and anionic Ag vacancies (V_{Ag}^{x} or V'_{Ag}), and neutral and cationic oxygen vacancies (V_{O}^{x} or $V_{O}^{\bullet}$ or $V_{O}^{\bullet\bullet}$) changed the local geometry in the vicinity of each defect. In particular, Ag_2O containing V_{Ag}^{x} vacancies exhibited a slight decrease in the length of the remaining Ag-O bonds to 2.092 Å, which was attributed to the anionic displacement toward the Ag ion in order to counterbalance the effect of dangling bonds. Similar results were founded for the defective Ag_2O unit cell containing V'_{Ag} that exhibited a more pronounced decrease in the length of the remaining Ag-O bonds to 2.077 Å. As a result, the local symmetry of O changed from the tetragonal arrangement in the non-defective bulk for a distorted trigonal planar.

On the other hand, the presence of V_{O}^{x} centers induced a higher distortion inside the Ag_2O matrix because the remaining Ag-O bonds became longer (2.223 Å), due to the cation displacement toward the central position of the tetrahedral, reducing the Ag-Ag bond length to 2.845 Å. Such effect is extremely important, in this case, both Ag cations are reduced from expulsion of the oxygen as neutral atom; the reminiscent electrons act as an one pair electrons coupled decrease the length bond creating a high condition to form a metallic Ag–Ag bond. In the presence of the $V_{O}^{\bullet}$, the results indicated Ag-O and Ag-Ag bonds equals to 2.213 Å and 2.901 Å, respectively; whereas, for the model with $V_{O}^{\bullet\bullet}$, the calculated Ag-O and Ag-Ag bond distances were 2.202 and 2.965 Å, respectively. Both oxygen cationic vacancies cause successive increase of the Ag–Ag bond length

because of the increase of the electrostatic repulsion between Ag and Ag ions unfavorable the metallic bond showed from V_O^x. This new structural rearrangement suggests that the formation of metallic Ag clusters inside the Ag_2O matrix can contain different V_O centers; however, only V_O^x presents minor Ag–Ag bond length and sufficient electrons to form metallic bond.

From now on we discuss the electronic structure of pristine and defective Ag_2O models based on the analysis of the density of states (DOS) and band structure profiles, presented in Figure 2. For pristine Ag_2O (Figure 2a), the valence band (VB) was composed of 4d Ag orbitals hybridized with O (2p) states, while the conduction band (CB) was mainly composed of empty 5s Ag orbitals. The band-gap was calculated as 2.07 eV, corresponding to a Γ-Γ direct transition, in good agreement with the experimental[20, 22-23, 55] and theoretical values.[55-57]

Figure 2

In contrast, the creation of V_{Ag}^x vacancies (Fig. 2b) induced the formation of intermediate levels in the band-gap region because of electron uncoupled reminiscent from vacancy localized between oxygens atoms, reducing the band-gap to 0.40 eV, between Γ and R points. This intermediate energy level is a flat band, contributing to the small difference between direct and indirect band-gap values (Fig. 2b). In the presence of V_{Ag} centers, the defects induced the creation of holes ($h^\bullet$) and a doublet ground state with metallic character, once the $h^\bullet$ is localized in the valence band maximum (VBM). After the reduction the V'_{Ag} (Fig. 2c) center becomes diamagnetic and the electronic structure returns to exhibit a semiconductor behavior with band-gap calculated as 2.15 eV, corresponding to a Γ-Γ direct transition. Therefore, with the creation of V_{Ag}^x the dangling bonds causes defect doublet states occupied by three electrons just above the VBM, acting as a shallow acceptor level. After the V_{Ag}^x reduction, the presence of the V'_{Ag} becomes the global electronic structure as a semiconductor behavior with diamagnetic nature showing an increased band-gap.

On the other hand, the presence of V_O^x centers (Fig. 2d) shifted the position of both VB and CB, increasing the band-gap value to 2.49 eV, between points Γ-Γ. This result

can be associated to the displacement of the oxygen with respect vacancy site with concomitant rearrangement of the electron density among the chemical bonds. This fact provokes changes on the upper part of the VB inducing a band-gap opening mechanism, once the Ag-O bonds are larger and the VBM are displace to a lower energy region. Similar results were found by Yin *et al*. where the creation of oxygen vacancies in Ag_2O induces an enlargement of the band-gap mainly for the perturbation in the upper part of the VB.[58]

For the neutral V_O^x, the removal of an O atom from the supercell model will result in four dangling bonds and the defect center occupy the lowest state found in the VB , while the unoccupied levels are found above the conduction band minimum (CBM), enabling to classify the V_O^x as a deep donor site. However, the V_O^x centers can be transformed into a positively charged vacancy, $V_O^{\bullet}$, by trapping a hole, while the remaining electron is trapped on the empty states of neighboring metal centers, resulting in a paramagnetic species. This fact was confirmed on band structure and DOS profiles (Fig. 2e), where an intermediary energy level was introduced in the band-gap region of Ag_2O confirming the paramagnetic nature of $V_O^{\bullet}$, that results in a reduced band-gap of 0.25 eV being an indirect transition between Γ-X points. As observed for V_{Ag}^x this intermediate energy level behaves as a flat band, contributing to the small difference between direct and indirect band-gap values (Fig. 2e).

In addition, one may expect that further ionization of $V_O^{\bullet}$ sites could produce double-positively charged $V_O^{\bullet\bullet}$ (Fig. 2f) centers showing a diamagnetic character, i. e. null magnetic moment from electrons coupled. Indeed, the electronic structure for this defect shows a non-magnetic behavior with a metallic character.

In particular, in order to determine the nature of the paired or unpaired electrons from the vacancy site remaining inside the Ag_2O matrix, we investigated the spin density of Ag_2O containing V_{Ag} centers, as shown in Figure 3.

Figure 3

In this case, it was noted that the creation of V_{Ag}^x centers (Fig. 3a) induces the redistribution of the remaining electron, which is mainly trapped on the neighboring Ag-O bond, resulting in reduced Ag species with unpaired electron occupation (S_z = 0.343)

on the $3d_{xz/yz}$, orbitals confirming the stabilization of doublet state. On the other hand, the creation of $V_O^{\bullet}$ centers (Fig. 3b) induces the localization of part of the unpaired spin inside the metallic Ag clusters (S_z = 0.214) inside the Ag_2O matrix summed to the delocalized unpaired electron density on the neighboring Ag-O bonds, being the electrons localized in the $3d_{xz/yz}$ orbitals of the Ag cation.

Therefore, the obtained results point out that the creation of V_{Ag}^{x} and $V_O^{\bullet}$ centers can be an effective tool to generate magnetic properties into non-magnetic Ag_2O matrix, explaining the observed experimental results reported so far.[59-63] In addition, such results can be helpful in future studies involving the observation of ferromagnetic behavior in commonly non-magnetic materials, a very interesting subject in the field of spintronic materials.

3.2. Electron-Hole Pair Mobility and Photocatalytic Activity

Photo-driven processes one of most promises since first quantum experiments to understand the light and matter interaction. The high energy concentration inside the photon is a great option to help the environmental treatment from new production or remediation processes. Recently, photocatalytic and photovoltaic devices have been extremely searched for applications in the conversion of energy from light, electricity (solar cells) or chemical (photocatalysis, water splitting, CO_2 reduction, and others) technologies[64] These technologies, require the knowledge on semiconductor electronic structure, which controls a complex sequence of events initiates from light adsorption process followed by the conduction of the photo-induced charge carriers and interaction with other chemical species. The general mechanism behind such processes can be separated in three steps: (i) light adsorption for automatically to generate the electron-hole (e'-h$^{\bullet}$) pair; (ii) charge carriers diffusion; (iii) the transference of the charge carrier to a molecule. In the first step, the energy of the light must be equal to or higher than the band-gap in order to promote an electron (e') from the VB to the CB, creating an electron vacancy in the VB, denoted as hole (h$^{\bullet}$). For solar-driven photocatalysis, the optimum band-gap ranges between 1.6 and 2.5 eV, this corresponds to the solar spectrum.[65-68] In this context, Ag_2O is a suitable candidate for solar-driven photocatalysis due to its band-gap of 2.07 eV (Figure 2a). The e'-h$^{\bullet}$ pair interacts through Coulomb attraction and plays a fundamental role in the subsequent steps, controlling the photocatalytic efficiency of

the semiconductor. In steps (ii) and (iii), the e' and h• must be separated to generate free charge carriers that are transported to active sites very well defined, where they will be active for photocatalysis before the recombination.[65]

The diffusion coefficient (*D*) reflects the mobility of a charge carrier, which in turn is linked to its effective mass (m^*). In particular, *D* increases as the effective mass of the photo-generated carrier decreases, resulting in an enhanced photocatalytic efficiency. Furthermore, the ratio between the effective masses of electrons (m_e^*) and holes (m_h^*) is a powerful tool to predict the stability of the e'-h• pair with respect to the recombination process. In this case, different effective mass for electrons and holes induces different mobilities for such charge carriers, reducing the e'-h• recombination rate and increasing the photocatalytic efficiency due to the structural separation.[65, 67-68] The effective mass can be associated with the curvature at the top of the VB or at the bottom of CB. For a single isotropic and parabolic band, the effective mass can be obtained as:

$$\frac{\mathbf{1}}{\boldsymbol{m}} = \frac{\mathbf{1}}{\hbar^2}\frac{\boldsymbol{\delta^2 E}}{\boldsymbol{\delta k^2}} \quad (6)$$

Therefore, the m_e^* and m_h^* values can be obtained by fitting the CBM and the VBM, respectively. This procedure was employed for other semiconductors and proved be very effective in predicting and rationalizing the photocatalytic activity.[69-72]

The calculated m_e^* and m_h^* values are summarized in Table 2. Equal m_e^* values were found along each direction in the reciprocal space, reflecting the isotropic nature of the CBM related to the hybridization of s orbitals, in agreement with other theoretical values reported in the literature.[55] In contrast, despite the overall similarity as regard the ration between the m_e^* and m_h^* values, the theoretical results reported by Wang *et al.*[20] shows different values when compared with the effective mass reported here and other theoretical results[55], probably due to the singularities involving the reproduction of the electronic structure at different exchange correlation functionals. On the other hand, the calculated m_h^* values were significantly different, suggesting different carrier mobilities along different directions. In fact, the holes were lighter along the (111) than the (110) and (100) directions, suggesting an increased mobility along (111) direction.

Table 2. Effective masses of the electron (m_e^*) and the hole (m_h^*) of Ag_2O obtained from parabolic fitting to the CBM and the VBM along each direction in the reciprocal space, respectively.

	Direction								
	X = (100)			M = (110)			R = (111)		
	m_e^*	m_h^*	m_h^*/m_e^*	m_e^*	m_h^*	m_h^*/m_e^*	m_e^*	m_h^*	m_h^*/m_e^*
Ag_2O	0.22	0.99	4.51	0.22	1.04	4.85	0.22	0.55	2.44
$Ag_2O{:}V_{Ag}^x$	0.20	2.74	13.47	0.19	1.04	5.39	0.19	0.38	2.04
$Ag_2O{:}V'_{Ag}$	0.21	1.08	5.24	0.20	1.07	5.46	0.19	0.65	3.46
$Ag_2O{:}V_O^x$	0.95	1.31	1.37	0.95	0.94	1.94	0.41	0.62	1.53
$Ag_2O{:}V_O^\bullet$	0.31	1.81	5.85	1.24	0.77	0.62	0.82	0.35	0.43

Our main discussion in this topic is devoted to the ratio between the effective mass of charge carriers reported in Table 2. Therefore, for pristine Ag_2O, regarding the e'-h$^\bullet$ recombination process, we argue that electrons and holes are more effectively separated along the (110) and (100) than the (111) surfaces, due to the higher m_h^*/m_e^* ratio. In particular, the present results indicate that the electron and hole mobilities along the (110) and (100) surfaces are very different and e'-h$^\bullet$ recombination rate is reduced suggesting that the photocatalytic process on these surfaces is enhanced.

Furthermore, it was noted that the creation of neutral V_{Ag}^x centers contributes to increase the m_e^*/m_h^* ratio along the X and M directions, while the ration for direction R is reduced. This fact indicates that superior photocatalytic properties can be associated to (100) and (110) surfaces due to the increased difference between the effective mass, indicating a reduced e'-h$^\bullet$ recombination rate. Similar results were found based on the existence of V'_{Ag} centers. Now, the e'-h$^\bullet$ recombination rate is reduced along all direction in comparison to pristine Ag_2O. In particular, the reduction and electron pairing that generate a diamagnetic ground state for V'_{Ag} reduces the m_h^*/m_e^* ratio along X direction. A combination of both results indicates that V_{Ag} centers contributes to increase the photocatalytic behavior of Ag_2O.

On the other hand, it was noted that the creation of both V_O^x and $V_O^\bullet$ centers does not contribute to increase the photocatalytic activity of Ag_2O once the m_h^*/m_e^* ratio is reduced along all direction in comparison to pristine Ag_2O. The exception occurs along the X direction for $V_O^\bullet$ centers, where the creation of a paramagnetic doublet state induces an increase of the charge carrier stability. Here, it is important to remark that the effective

mass were not considered for the model including $V_O^{\bullet\bullet}$ centers due to the metallic behavior observed in the Figure 2.

An especial point can be visualized from Table 2 involving the V_{Ag}^{x} and $V_O^{\bullet}$ centers. For both models, it was observed an increased m_h^*/m_e^* ratio along the X direction as compared to pristine Ag_2O. This fact indicates that the unpaired spin observed for these models is mainly located along a selected region on the reciprocal space exhibiting a singular behavior as regard the carriers diffusion along the electronic structure. Such unpaired spin is a source to make an Ag – Ag metallic bond.

3.3. Surfaces and Morphology

To disentangle electronic and structural effects, first, we fully optimized the low-index (100), (110), and (111) Ag_2O surfaces to investigate the relation between E_{surf} and crystal morphology. Table 3 summarizes the values of E_{surf}, band-gap, and density of dangling bonds for each surface.

Table 3. Calculated surface energy values (E_{surf}), band-gap, dangling bonds, area and dangling bond density (D_b) for (100), (110) and (111) surfaces of Ag_2O.

Surfaces	**E_{surf} (J/m²)**	**Band-gap (eV)**	**Dangling bonds**	**Area (nm²)**	**D_b (nm^{-2})**
(100)	1.58	metal	4	0.2351	17.01
(110)	1.33	metal	4	0.3325	12.03
(111)	0.74	2.26	4	0.4072	9.82

The stability order decrease as follows:(111) > (110) > (100), reflecting the dangling bond density on the surfaces, in agreement with previous theoretical results.[20] In this case, the main differences when compared with the values reported by Wang *et al.* can be addressed to the method used in both studies, once the value of E_{surf} surface is dependent of the exchange-correlation functional.[73] In particular, the (111) surface exhibited a lower dangling bond density compared with that of the (110) and (100) surfaces. The differences between the E_{surf} values of the (110) and (100) surfaces can be mainly ascribed to the different dangling bond density at the exposed O_{3c} and O_{2c} centers in the upper part of the slabs representing(110) and (100) surfaces, respectively.

The above order of stability can be rationalized by analyzing the atomic rearrangements at the exposed surfaces, as illustrated in Figure 4, which shows the optimized geometries of the investigated surfaces. In this figure, we used a Kröger-Vink notation[40] to describe describe both V_O^x and and distorted clusters ($[AgO_n]_{distorted}$). Here, it is important to clarify that structural distortions does not include the creation of new chemical bonds that describe the surface reconstruction mechanism.

Figure 4

The most stable surface was found as a non-polar (111) one, for which symmetric and stoichiometric slabs were obtained, resulting in a zero dipole moment perpendicular to the surface plane. Figure 4c displays the exposed $[Ag_2O]_{distorted}$ clusters; the main difference with respect to the bulk was attributed to local disorder associated with angular distortions (O-Ag-O < 180°), which induced a redistribution of the electronic density on this surface.

On the other hand, both (100) and (110) surfaces were asymmetrical and exposed different chemical environments, i.e., the upper and lower part of the slabs were composed of different clusters. In both cases, regular $[AgO_2]$ clusters similar to the bulk appeared on the upper part of the slab model, whereas the lower part of the slab contained defective centers, described as $[AgO\ldots V_O^x]$ units.The (110) plane contained O_{3c} centers in the upper part of the slab, while the (100) surface exhibited oxygen anions surrounded by two Ag atoms (O_{2c}). Therefore, the (110) surface showed higher stability because its exposed planes were more similar to the bulk system.

By analyzing the undercoordinated and distorted clusters of each exposed surface, we can propose that the balance between attractive and repulsive forces controls the energetics and electronic structure on Ag_2O surfaces. The photo-induced properties of materials reflect their electronic band structure, in terms of valence position, conduction band edges, and Fermi level. In particular, the Fermi level represents the chemical or electrochemical potential of electrons, and its precise understanding is essential to correlate the electronic band structure and the charge transfer characteristics of the materials. In this context, the properties responsible for the photocatalytic processes can be tuned by controlling the exposed surfaces, which can affect the redox abilities of photo-

induced carriers through the morphology and composition of the material.[74-76] In this study, the electronic structure of the Ag_2O surfaces was investigated through the DOS analysis shown in Figure 5.

Figure 5

The analysis of the results reveals that the (111) surface exhibited a band-gap around 2.26 eV, showing a similar semiconducting behavior to that observed for the bulk (Figure 2), whereas both (100) and (110) surfaces became metallic, suggesting an increased reactivity. The experimental investigations of the facet-dependent electrical conductivity by Tan *et al.*[74] showed that the (111) facet is the most conductive surface, followed by the (100) and (110) ones: this represents an opposite trend with respect to the present theoretical results. However, the authors also reported that the thickness of the thin surface layer results in facet-dependent properties, which is the fundamental reason for the observed discrepancy with our results.[77]

In order to elucidate the relation between surface morphology and photocatalytic properties of Ag_2O, the Wulff construction was employed to obtain the equilibrium morphology of Ag_2O based on the calculated values of E_{surf} for the (100), (110), and (111) surfaces, as shown in Figure 6. In addition, different morphologies could be obtained by changing the ratio between the E_{surf} values of each surface. Such transformations between the different morphologies are associated with geometric constraints imposed by the crystal structure and the relative E_{surf} values of each surface.[46, 50, 78]

Figure 6

The ideal morphology of Ag_2O exhibited an octahedral shape that predominantly exposed the (111) surface, according to thermodynamic criteria based on the values of E_{surf}, in agreement with experimental evidences. By varying the ratio between the E_{surf} values of the (111) and (100) surfaces, different morphologies could be obtained, such as truncated octahedral and different rhombicuboctahedral ones, matching the experimental morphologies obtained by examining the SEM images.[20, 22] In addition, cubic and truncated (corner and edge)-cubic morphologies were obtained by controlling the ratio

between the E_{surf} values of the (100) and (110) surfaces, whereas changing the ratio between the (110) and (111) surface energies allowed obtaining edge-truncated octahedral and rhombic dodecahedra shapes. It is important to point out that the theoretical morphologies obtained from Wulff construction show an excellent agreement with the experimental images obtained by SEM.[20, 22]

The next goal was determine the connection between the morphologies of the Ag_2O samples and their photocatalytic activities. Wang *et al.* investigated different Ag_2O samples and reported that the cubic morphology exhibited the highest degradation rate, followed by rhombicuboctahedral and edge/corner-truncated cubic shapes. [20] The authors also showed that Ag_2O microcrystals with exposed (100) facets displayed superior photocatalytic performance.[20] Similar results were reported by Chen *et al.*, who compared cubic, octahedral, and rhombic dodecahedral shapes based on their facet-dependent photodegradation of methyl orange, and found that the cubic shape had the highest photocatalytic activity.[22]

Based on the analysis of the surface morphology and carrier mobility results presented in Figure 6 and Table 2, respectively, we argue that the photocatalytic activity increases with the exposure of both (100) and (110) surfaces, due to the increased separations between e'-h$^{\bullet}$ pair, which reduces the recombination rate. This result is supported by experimental evidences showing that the cubic, rhombicuboctahedral, and edge/corner-truncated Ag_2O shapes predominantly expose (100) and (110) surfaces with higher photocatalytic activity.[20]

Figure 7

From a thermodynamic point of view, the morphology is controlled by relative stability of the different surfaces, and the surface with the lowest E_{surf} value is the main component of the corresponding morphology. Surfaces with larger E_{surf} values are important for improving the photocatalytic reactivity, but their proportion is expected to decrease rapidly during the crystal growth process, due to the minimization of E_{surf}. Therefore, the surface-controlled synthesis of crystals is a very robust procedure to study connections between surface structure, morphology, and photocatalytic properties, and also a feasible method to develop highly active photocatalysts. Changing the growth

conditions of the crystals (i.e., presence of surfactant and/or solvent) results in a different crystal morphology.

Adjusting the ratio of the E_{surf} values of the three surfaces is allowed obtaining different morphologies, and the corresponding reaction paths can be isolated and studied independently. This procedure can be considered an effective tool to investigate the mechanisms of morphology transformation and crystal growth from a thermodynamic and kinetic point of view[10] and can provide useful insights for making Ag_2O materials with morphologies suitable for a wide variety of specific devices and purposes.

Figure 7 shows three different reaction paths starting from the ideal morphology of Ag_2O. In reaction path (A), a rhombicuboctahedral shape was obtained via truncation of the octahedral morphology in order to predominantly expose the highly reactive (100) and (110) surfaces, with a minor proportion of (111) surfaces. In terms of the thermodynamic stability associated with E_{pol} (Supplementary Information, Table S1), the final morphology showed a rather similar stability to the ideal octahedral shape. In reaction path (B), two potential photocatalytic morphologies (cubic and edge/corner-truncated cubic), exposing mainly the (100) and (110) surfaces, were obtained by truncation at both the edge and corner sides of the ideal octahedral shape. The obtained cubic shape, which was exposed only (100) surfaces, showed a lower E_{pol} than the ideal Ag_2O shape, denoting a higher stability, which would make it suitable for photocatalytic applications. Finally, in reaction path (C), morphologies with higher E_{pol} were obtained by truncation of the octahedral ideal shape because of the stabilization of the (110) surface to generate rhombic dodecahedral shapes. Therefore, along both reaction paths (A) and (B), the most stable shapes (rhombicuboctahedral and cubic) exhibited higher proportions of both (100) and (110) surfaces, and were the most promising candidates with enhanced photocatalytic activities. When the proportion of the (111) surface increased with respect to the (100) and (110) ones, the photocatalytic activity of the corresponding morphology decreased, suggesting that the (100) and (110) surfaces are more photocatalytically active than the (111) surface.

3.4 Photocatalytic Mechanism of Ag_2O

In this section, we propose a general photocatalytic mechanism connecting the crystal morphology and electronic structure of Ag_2O. Different crystal surfaces exhibit

distinct VBM and CBM energy levels, due to the different atomic arrangements exposed on the surfaces. This difference can directly lead to the localization of photo-induced e'-h• pairs, favoring their separation and reducing the e'-h• pair recombination rate. Figure 5 shows the DOS profiles of both bulk Ag_2O and Ag_2O surfaces, revealing that the VBM maxima of the (100) and (110) surfaces were shifted at higher energies with respect to those of the (111) surface and Ag_2O bulk. Therefore, we can argue that h• centers will accumulate on (100) and (110) surfaces, while electrons will migrate to the energetically favorable (111) plane. In order to confirm these results, we calculated the atomic charges for both Ag and O atoms using the Mulliken charge (Supplementary Information, Table S2). In this context, it is important to remark that Mulliken charge is used to disclose the local charge accumulation/depletion for the excited states in comparison to the fundamental ground state. In bulk Ag_2O, the Ag and O centers possessed net charges of 0.44 and -0.84 |e|, respectively. The charge values obtained for the different Ag_2O surfaces (reported in Table S2) support the DOS analysis, as both (100) and (110) surfaces showed an increased net charge for Ag centers, while the exposed Ag centers on the (111) surface had a reduced net charge; this confirms the accumulation of positive charge on the (100) and (110) surfaces, associated with the presence of h• centers, while electrons are mainly trapped on (111) surface.

The above discussion is entirely based on the Kohn-Sham energy levels of the ground state of the system. However, photocatalytic activity is an excited electronic state problem, which requires going beyond the one-electron approximation. The main changes in the fate of the photo-generated carriers during the transformations between fundamental, s, and excited, s*and t*, electronic states were investigated by explicitly computing the electronic transition forcing the electronic structure of the system into s* or t* electronic state, which we assumed to approximate an excited state of the system. This approximation is valid in the limit of weakly interacting electrons. Starting from the ground-state geometry, we optimized the electronic structure in its singlet or triplet electronic state. Therefore, to determine the photo-induced mechanism relevant for Ag_2O, we localized and characterized the excited s* and t* electronic states after the photonic excitation of electrons located on the VBM. The geometries of these excited electronic states are described in Table 4, while the calculated vibrational properties are presented in Table S3 of the Supplementary Information.

Table 4. Theoretical lattice parameters and bond lengths for Ag_2O at excited singlet (s*) and triplet (t*) states.

	Lattice Parameters			Bond Distances	
	a (Å)	**b (Å)**	**c (Å)**	**Ag-O (Å)**	**Ag-Ag (Å)**
*s**	4.879	4.879	4.789	2.099 (2x)	3.418
*t**		4.899		2.122 (2x)	3.465

The main changes taking place during the transformations between s, s*, and t* states are presented in Figure 8. The pathway from s ground state to s* excited state involved a slight tetragonal distortion that reduced the *z*-axis lattice parameter as well as the Ag-O and Ag-Ag bond distances. This electronic transition was followed by the appearance of new vibrational modes (Supplementary Information, Table S2) at a 254.74 cm^{-1} frequency, associated with the main structural deformations that connected s and s* states from the crystalline distortion of the Ag cations and their O neighbors. The pathway connecting the s* and t* excited states involved a structural rearrangement that restored the cubic symmetry through a unit cell expansion accompanied by increases in the Ag-O and Ag-Ag bond distances. In this case, the calculated vibrational modes are in agreement with the group symmetry analysis for cubic Ag_2O, which showed only one active Raman mode (F_{2g}) corresponding to the bending motion of the O-Ag-O moiety. In the final step, the decay process from t* to s involved reduction of the lattice parameters, which resulted in shorter Ag-O and Ag-Ag bond distances.

Figure 8

The main changes involving the (100), (110) and (111) surfaces were evaluated using the E_{surf} values of both s* and t* excited states. For the s* excited state, the obtained results indicate that the (100), (110), and (111) surfaces had E_{surf} values of 1.68, 1.53, and 0.78 J/m², respectively. These values were higher than the corresponding values of E_{surf}

for the ground state (Table 3), which can be attributed to the geometrical constraint observed in bulk s* models, where a tetragonal distortion was found. The results of the charge analysis (Table S2) show similar calculated values to those of the ground state (s), confirming the e'-h• pair separation.

On the other hand, the calculated E_{surf} values for the t* electronic state were 1.32J/m² for (111), 1.63 J/m² for (110), and 1.70 J/m² for (100). In this case, the main changes, in particular for the (111) surface, could be associated to the electronic structure, because our previous results indicated that the photo induced e' and h• centers were separated along the (100), (110), and (111) surfaces. The calculated charges (Table S2) indicate an enhanced separation of the charge carriers (e'-h•). In fact, both (100) and (110) surfaces showed the highest values of net charge for Ag centers, confirming the accumulation of positive h• centers in the upper part of the slab, while the (111) surface exhibited highly reduced Ag centers, resulting from the accumulation of photo-induced e' on this plane.

In order to examine the nature of unpaired electrons in both bulk and surface states of Ag_2O, the spin isosurfaces for the t* electronic state are plotted in Figure 9. Here, we can argue that spin density distribution combined with the previous reported Mulliken charge analysis can be used to elucidate the mechanism associated with the localization of both e' and h• on each surface termination. The results for bulk Ag_2O indicate that the excited electrons were trapped on the Ag ($S_z = 0.361$) cations located on the (111) surface, resulting in reduced [Ag_2O] clusters. On the other hand, both (100) and (110) surfaces showed a different spin density distribution in the upper and lower parts of the slab. In both cases, the upper part consisted of reduced O [$S_z = 0.919$ for (100) and $S_z = 0.217$ for (111)] centers with increased spin density compared with the bulk, whereas the lower region exhibited charge accumulation on the exposed Ag cations with reduced coordination, [AgO...V_O^x], where V_O^x correspond to an oxygen vacancy. The calculated spin density suggests the formation of reduced [AgO_2] clusters on the (111) surface, confirming that the excited electrons were mainly trapped in the electronic states exposed on this plane, as also observed for bulk [Ag_2O] in the t* state, where magnetic Ag^0 centers ($S_z = 0.376$) can be located on (111) surface. Therefore, from the obtained results photo-induced mechanism involving the presence excited states and charge density redistribution can be proposed.

Figure 9

To analyze the electronic structure of the excited s* and t* electronic states, the DOS profiles for both bulk and surface models are presented in Figure 10.

Figure 10

The results for s* excited electronic state in Figure 10a,c indicate a slight perturbation in the VBM and CBM, with band-gap values of 2.06 and 2.24 eV for bulk and (111) surface, respectively. On the other hand, the DOS profiles for t* excited electronic state (Figure 10b,d) indicate that the spin separation along the crystalline structure promoted a non-degenerate spin distribution in the vicinity of the VBM for both bulk and (111) surface. In fact, for (111) surface model, a localized electronic state was identified in the upper part of the VB, corresponding to the electrons of the Ag-O bond. In this case, it should be noted that the band-gap for excited bulk model is similar to previously discussed values, showing an excitation around 2.03 eV, whereas the (111) surface presented a reduced band-gap value around 1.61 eV. The above results can be attributed to the e' - h$^{\bullet}$ pair separation process after the photo-induced excitation, owing to the reduced band-gap values for the (111) surface in the excited t* electronic state; then, the photoexcited e' centers were mainly trapped in the clusters exposed on (111) surface, while the h$^{\bullet}$ centers were located in the bulk and in the metallic (100) and (110) surfaces. Those facts confirms the aftermentioned properties evaluated by means of Mulliken charge analysis and spin density distribution, confirming that the simulation of excited states plays a fundamental role on the understanding of photo-induced properties.

An additional information about the surface reactivity can be addressed to the Hard or Soft character of acid/bases (HSAB). Here, such information was computed by considering the Chemical Hardness (η) of the Ag_2O surfaces, considering that η can be computed as the difference between LUMO (CBM) and HOMO (VBM) frontiers crystalline orbitals in the framework of Koopaman's Theorem.[79] In the fundamental ground state the chemical hardness of (100), (110) and (111) surfaces were calculated as

0.0, 0.0 and 2.26 eV, respectively. Therefore, (100) and (110) surfaces are soft in comparison with (111). However, for the excited s* and t* states the chemical hardness of (100) and (110) was maintained, while the calculated values for (111) surface (2.24 eV and 1.61 eV) indicates a softening behavior.

From a fundamental point of view, the photocatalytic generation of radical species can be considered as a redox process. Therefore, both oxidation and reduction sites need to be located on the reactive and exposed surfaces. In this context, the electronic band structure of a semiconductor photocatalyst can be tuned by exposing specific surfaces, with a significant impact on the redox abilities of photo-induced carriers.[80-84] As discussed above, the first step in the photocatalysis mechanism is the photo-induced electronic transition following absorption of light with energy equal to or greater than the band-gap energy of Ag_2O; the transition generates an e' - h$^{\bullet}$ pair, following the reaction described in the Equation 7. In this case, the superscript "x" correspond to the neutral nomenclature of Kröger-Vink notation, while subscripts "o" and "d" nomenclature refers to the existence of both ordered and distorted clusters, respectively.

$$[AgO_2]_o^x + [AgO_2]_d^x + h\upsilon \rightarrow [AgO_2]_d' + [AgO_2]_d^{\bullet} \quad (7)$$

Where, $[AgO_2]_d'$ cluster is connected to e' charge carrier, and $[AgO_2]_d^{\bullet}$ cluster is linked to h$^{\bullet}$ charge carrier.

The next step corresponds to the migration process of the e' and h$^{\bullet}$ charge carriers to the exposed surfaces of Ag_2O. In this step, the calculated effective masses for e' and h$^{\bullet}$ indicate different charge carrier mobilities along different planes, suggesting that the oxidation sites are mainly located on the (100) and (110) surfaces, due to the accumulation of holes, while the reduction sites are located on the (111) surface, due to the presence of electrons.

Based on the above results, we propose that the surface structure associated with the exposure of undercoordinated species is a fundamental factor behind the separation of charge carriers. In fact, the DOS results for both ground and excited states indicate that the (111) surface accumulates excited electrons, due to the presence of regular $[AgO_2]$ clusters that become distorted after the photo-induced excitation following the capture of the excited e' species, generating $[AgO_2]_d'$ centers.

On the other hand, the h• centers generated at the VBM are trapped in the electronic states of the clusters exposed on the (100) and (110) surfaces. In both cases, the lower part of the modeled slab showed a defective center created upon surface exposure that can be described as an oxygen-deficient [AgO…V_O] cluster; the latter can act as trapping center for the photo-generated hole, according to the following process:

$$[AgO_2]_d^x \rightarrow [AgO...V_o^x] + 1/2\ O_2 \quad (8)$$

$$[AgO_2]_d^x + [AgO...V_o^x] \rightarrow [AgO_2]_d' + [AgO...V_o^\bullet] \quad (9)$$

Based on these results, we propose a photocatalytic mechanism where the exposed clusters on the Ag_2O surfaces can act as active sites, generating the reactive species according to the following reactions:

$$[AgO...V_o^\bullet] + H_2O \rightarrow \left[AgO...V_o^x\right] + OH^\bullet + H^\bullet \quad (10)$$

$$[AgO_2]_d' + O_2 \rightarrow [AgO_2]_d^x + O_2' \quad (11)$$

$$O_2 + H^\bullet \rightarrow O_2H^\bullet \quad (12)$$

$$O_2' + OH^\bullet + O_2H^\bullet + \text{organic compounds} \rightarrow CO_2 + H_2O + \text{degradation products} \quad (13)$$

Different [AgO...V_O^x] and $[AgO_2]_d'$ clusters, observed on the upper part of the Ag_2O surface, can adsorb H_2O and O_2 molecules in order to generate hydroxyl radical, $OH^\bullet$, hydrogen radical, $H^\bullet$, superoxide radical, O_2', and peroxide radical, $O_2H^\bullet$ as reactive species. This scenario is similar to the main ideas discussed by Jiang *et al*. to explain the mechanism and the superior photocatalytic properties of Ag_2O.[55]

The sequence of reactions involved in the photocatalytic process, outlined in Equations 8–13, were proposed on our previously commented results, taking into account the Ag_2O morphology and electronic structure presented in Figure 11. Here, we considered the rhombicuboctahedral Ag_2O morphology, due to its superior photocatalytic properties with the presence of the (100), (110), and (111) exposed surfaces.

Figure 11

In a first step, light adsorption generates e' and h• centers, which are separated along of a spontaneous migration from bulk to Ag_2O surfaces, according to the VBM energy levels and the effective masses of electrons and holes (Table 2 and Figure 6). In the next step, e' and h• active centers react with adsorbed species generating different kinds of radicals, which are responsible by degradation of organic compounds into carbon dioxide (CO_2) and water (H_2O). Therefore, we argue that (100) and (110) can absorb more easily H_2O to generate $OH^•$ and $H^•$ radicals, while (111) can act as a adsorption center to O_2 in order to generate O'_2 and $O_2H^•$ radicals.

Therefore, different exposed surfaces can induce distinct photocatalytic activities, depending on the nature of the exposed charge carriers in the Ag_2O morphology. In addition, morphologic modulation represents an excellent tool to achieve enhanced photocatalytic activities.

4. Conclusions

In order to elucidate the connection between crystal morphology, electronic structure, and photocatalytic activity, we carried out first-principles DFT calculations on appropriate bulk and surface models of Ag_2O, for both ground and excited electronic states. The theoretical results reveal the electronic structure of both pure and defective Ag_2O, indicating that photo-generated e' and h• exhibit distinct paths for mobility along of different crystallographic directions; in particular, (100) and (110) planes show the highest carrier stabilization, due to the increased ratio between the effective masses of e' and h•. In particular, it was proved that both neutral and charged V_{Ag} defects shows an favorable influence on the photocatalytic behavior of Ag_2O once the recombination rate between electrons and holes increased. Different morphologies were constructed by tuning the E_{surf} values for the (100), (110), and (111) surfaces, and were found in excellent agreement with the experimental results. Combined with the results of previous photocatalytic experiments, we found how Ag_2O crystals with exposed (100) and (110) surfaces enhance the photocatalysis process, enabling the photo-generated carriers to be used for effectively generate radical species. A combination of different theoretical tools allowed us to understand the nature of the superior photocatalytic behavior of some Ag_2O morphologies, and thus represents an interesting protocol to investigate other semiconductor photocatalysts. The two low-energy (100) and (010) surfaces are

dominant in the Wulff shape. The high surface energy and the obvious surface relaxation of the Ag_2O (001) surface indicate its high photocatalytic activity, which is in accordance with other experimental results. The present picture, obtained by considering realistic atomistic models of bulk Ag_2O and its surfaces, along of explicit electronic excitations involving ground and excited electronic states, singlet and triplet, is fully consistent with the experimental evidence.

One of more important promises to minimize the human action on world climate is the use of the semiconductors oxides as photocatalyst agent. Heterogeneous photocatalysis is great option to environmental remediation due to easy separation and recuperation of the photocatalyst agent.

In summary, our study illustrate, for the first time, the great potential of first principle calculations for developing semiconductors and design highly efficient photocatalysts based on Ag_2O material, and offers offering important clues for the development of singlet-triplet electronic states involved in photocatalytic activity under visible light irradiation and improve the photocatalytic activity of Ag_2O surfaces, in agreement with existing experimental observations. Our work also provides insight and guidance for tuning optoelectronic properties of Ag_2O materials.

Acknowledgments

This work was supported by the Federal University of São Carlos, Federal University of Rio Grande do Norte (*PPGCEM-UFRN*), State University of Ponta Grossa, University of Jaume I, CAPES, PDSE-CAPES, CNPq, and Fundação Araucária (Brazil). R. A. P. Ribeiro acknowledges financial support from CNPq 156176/2018-1. M. C. Oliveira acknowledges the financial support from *PNPD/CAPES* (2019/88887.319041). J. Andrés acknowledges Universitat Jaume I for project UJIB2016-25, Generalitat Valenciana for projects PrometeoII/2014/022, ACOMP/2014/270, and ACOMP/2015/1202, as well as Ministerio de Economia y Competitividad (Spain) ProjectCTQ2015-65207-P for financial support. E. Longo acknowledges financial support from FAPESP 2013/07296-2. The authors thanks to Enio Longo for the support with the scientific illustrations.

References

1. Ravelli, D.; Dondi, D.; Fagnoni, M.; Albini, A., Photocatalysis. A multi-faceted concept for green chemistry, *Chemical Society Reviews* **2009,** 38 (7), 1999-2011.
2. Gaya, U. I.; Abdullah, A. H., Heterogeneous photocatalytic degradation of organic contaminants over titanium dioxide: A review of fundamentals, progress and problems, *Journal of Photochemistry and Photobiology C: Photochemistry Reviews* **2008,** 9 (1), 1-12.
3. Schneider, J.; Matsuoka, M.; Takeuchi, M.; Zhang, J.; Horiuchi, Y.; Anpo, M.; Bahnemann, D. W., Understanding TiO_2 Photocatalysis: Mechanisms and Materials, *Chemical Reviews* **2014,** 114 (19), 9919-9986.
4. Carp, O.; Huisman, C. L.; Reller, A., Photoinduced reactivity of titanium dioxide, *Progress in Solid State Chemistry* **2004,** 32 (1), 33-177.
5. Hernandez-Alonso, M. D.; Fresno, F.; Suarez, S.; Coronado, J. M., Development of alternative photocatalysts to TiO_2: Challenges and opportunities, *Energy & Environmental Science* **2009,** 2 (12), 1231-1257.
6. Zhao, Y.; Eley, C.; Hu, J.; Foord, J. S.; Ye, L.; He, H.; Tsang, S. C. E., Shape-Dependent Acidity and Photocatalytic Activity of Nb_2O_5 Nanocrystals with an Active TT (001) Surface, *Angewandte Chemie International Edition* **2012,** 51 (16), 3846-3849.
7. Singh, S.; Barick, K. C.; Bahadur, D., Shape-controlled hierarchical ZnO architectures: photocatalytic and antibacterial activities, *CrystEngComm* **2013,** 15 (23), 4631-4639.
8. Xiao, X.; Liu, X.; Zhao, H.; Chen, D.; Liu, F.; Xiang, J.; Hu, Z.; Li, Y., Facile Shape Control of Co_3O_4 and the Effect of the Crystal Plane on Electrochemical Performance, *Advanced Materials* **2012,** 24 (42), 5762-5766.
9. Yuhang, X.; Xiangyu, Z.; Hongbo, Z.; Mengjie, Z.; Shuo, M.; Chunhui, S.; Shao, J., Luminescence properties of Eu^{3+} doped $BaMoO_4$ transparent glass ceramics, *J. Non-Cryst. Solids* **2018,** 500, 243-248.
10. Macedo, N. G.; Gouveia, A. F.; Roca, R. A.; Assis, M.; Gracia, L.; Andrés, J.; Leite, E. R.; Longo, E., Surfactant-Mediated Morphology and Photocatalytic Activity of α-Ag_2WO_4 Material, *The Journal of Physical Chemistry C* **2018,** 122 (15), 8667-8679.
11. de Oliveira, R. C.; de Foggi, C. C.; Teixeira, M. M.; da Silva, M. D. P.; Assis, M.; Francisco, E. M.; Pimentel, B. N. A. d. S.; Pereira, P. F. d. S.; Vergani, C. E.; Machado, A. L.; Andres, J.; Gracia, L.; Longo, E., Mechanism of Antibacterial Activity via Morphology Change of α-$AgVO_3$: Theoretical and Experimental Insights, *ACS Applied Materials & Interfaces* **2017,** 9 (13), 11472-11481.
12. Zhang, C.; Zhang, H.; Zhang, K.; Li, X.; Leng, Q.; Hu, C., Photocatalytic Activity of $ZnWO_4$: Band Structure, Morphology and Surface Modification, *ACS Applied Materials & Interfaces* **2014,** 6 (16), 14423-14432.
13. Huang, M. H.; Naresh, G.; Chen, H.-S., Facet-Dependent Electrical, Photocatalytic, and Optical Properties of Semiconductor Crystals and Their Implications for Applications, *ACS Applied Materials & Interfaces* **2018,** 10 (1), 4-15.
14. Peng, Y.-K.; Tsang, S. C. E., Facet-dependent photocatalysis of nanosize semiconductive metal oxides and progress of their characterization, *Nano Today* **2018,** 18, 15-34.
15. Oliveira, C. A.; Volanti, D. P.; Nogueira, A. E.; Zamperini, C. A.; Vergani, C. E.; Longo, E., Well-designed β-Ag_2MoO_4 crystals with photocatalytic and antibacterial activity, *Materials & Design* **2017,** 115, 73-81.

16. Byzynski, G.; Melo, C.; Volanti, D. P.; Ferrer, M. M.; Gouveia, A. F.; Ribeiro, C.; Andrés, J.; Longo, E., The interplay between morphology and photocatalytic activity in ZnO and N-doped ZnO crystals, *Materials & Design* **2017,** 120, 363-375.
17. Bai, S.; Wang, L.; Li, Z.; Xiong, Y., Facet-Engineered Surface and Interface Design of Photocatalytic Materials, *Advanced Science* **2017,** 4 (1), 1600216.
18. Wang, H.; Qiao, L.; Xu, H.; Lin, Y.; Shen, Y.; Nan, C., Anisotropy of Photocatalytic Properties in Nanostructured Photocatalysts, *Soft Nanoscience Letters* **2016,** 06 (02), 11-30.
19. Ida, Y.; Watase, S.; Shinagawa, T.; Watanabe, M.; Chigane, M.; Inaba, M.; Tasaka, A.; Izaki, M., Direct Electrodeposition of 1.46 eV Bandgap Silver(I) Oxide Semiconductor Films by Electrogenerated Acid, *Chemistry of Materials* **2008,** 20 (4), 1254-1256.
20. Wang, G.; Ma, X.; Huang, B.; Cheng, H.; Wang, Z.; Zhan, J.; Qin, X.; Zhang, X.; Dai, Y., Controlled synthesis of Ag_2O microcrystals with facet-dependent photocatalytic activities, *Journal of Materials Chemistry* **2012,** 22 (39), 21189-21194.
21. Yeu-Wei, H.; Tung-Han, Y.; Tsung-Yeh, T.; Miao-Chun, C.; Jenn-Ming, W., Facet-Dependent Photocatalytic Activity and Facet-Selective Etching of Silver(I) Oxide Crystals with Controlled Morphology, *ChemCatChem* **2015,** 7 (1), 80-86.
22. Chen, Y.-J.; Chiang, Y.-W.; Huang, M. H., Synthesis of Diverse Ag_2O Crystals and Their Facet-Dependent Photocatalytic Activity Examination, *ACS Applied Materials & Interfaces* **2016,** 8 (30), 19672-19679.
23. Chih-Shan, T.; Ying-Jui, C.; Chi-Fu, H.; H., H. M., Facet-Dependent Electrical Conductivity Properties of Silver Oxide Crystals, *Chemistry – An Asian Journal* **2017,** 12 (3), 293-297.
24. Kim, M.-J.; Cho, Y.-S.; Park, S.-H.; Huh, Y.-D., Facile Synthesis and Fine Morphological Tuning of Ag_2O, *Crystal Growth & Design* **2012,** 12 (8), 4180-4185.
25. Yan, D.; Li, Y.; Huo, J.; Chen, R.; Dai, L.; Wang, S., Defect Chemistry of Nonprecious-Metal Electrocatalysts for Oxygen Reactions, *Advanced Materials* **2017,** 29 (48), 1606459.
26. Wang, G.; Yang, Y.; Han, D.; Li, Y., Oxygen defective metal oxides for energy conversion and storage, *Nano Today* **2017,** 13, 23-39.
27. Qingmen, W.; Mengting, S.; Bing, Z.; Kang, Z.; Huanhuan, L.; Longfei, M.; Yang, J.; Yan, R.; Junling, C.; Yingcui, F., Strong damping of the localized surface plasmon resonance of Ag nanoparticles by Ag_2O, *Nanotechnology* **2018,** 29 (29), 295702.
28. Wang, X.; Li, S.; Yu, H.; Yu, J.; Liu, S., Ag_2O as a New Visible-Light Photocatalyst: Self-Stability and High Photocatalytic Activity, *Chemistry – A European Journal* **2011,** 17 (28), 7777-7780.
29. Zhou, W.; Liu, H.; Wang, J.; Liu, D.; Du, G.; Cui, J., Ag_2O/TiO_2 Nanobelts Heterostructure with Enhanced Ultraviolet and Visible Photocatalytic Activity, *ACS Applied Materials & Interfaces* **2010,** 2 (8), 2385-2392.
30. Tjeng, L. H.; Meinders, M. B. J.; van Elp, J.; Ghijsen, J.; Sawatzky, G. A.; Johnson, R. L., Electronic structure of ${\mathrm{Ag}}_{2}$O, *Physical Review B* **1990,** 41 (5), 3190-3199.
31. Hoflund, G. B.; Hazos, Z. F.; Salaita, G. N., Surface characterization study of Ag, AgO, and ${\mathrm{Ag}}_{2}\mathrm{O}$ using x-ray photoelectron spectroscopy and electron energy-loss spectroscopy, *Physical Review B* **2000,** 62 (16), 11126-11133.
32. Allen, J. P.; Scanlon, D. O.; Watson, G. W., Electronic structures of silver oxides, *Physical Review B* **2011,** 84 (11), 115141.

33. Aniruddha, D.; Arun Kumar, C., The electronic structure and chemical bonding mechanism of silver oxide, *Journal of Physics: Condensed Matter* **1998,** 10 (50), 11719.
34. Behrens, P.; Aßmann, S.; Bilow, U.; Linke, C.; Jansen, M., Electronic Structure of Silver Oxides Investigated by AgL XANES Spectroscopy, *Zeitschrift für anorganische und allgemeine Chemie* **1999,** 625 (1), 111-116.
35. Gordienko, A. B.; Zhuravlev, Y. N.; Fedorov, D. G., Band structure and chemical bonding in Cu_2O and Ag_2O oxides, *Physics of the Solid State* **2007,** 49 (2), 223-228.
36. Umezawa, N.; Shuxin, O.; Ye, J., Theoretical study of high photocatalytic performance of Ag${}_{3}$PO${}_{4}$, *Physical Review B* **2011,** 83 (3), 035202.
37. Dovesi, R.; Orlando, R.; Erba, A.; Zicovich-Wilson, C. M.; Civalleri, B.; Casassa, S.; Maschio, L.; Ferrabone, M.; De La Pierre, M.; D'Arco, P.; Noël, Y.; Causà, M.; Rérat, M.; Kirtman, B., CRYSTAL14: A program for theab initioinvestigation of crystalline solids, *International Journal of Quantum Chemistry* **2014,** 114 (19), 1287-1317.
38. Adamo, C.; Barone, V., Toward reliable density functional methods without adjustable parameters: The PBE0 model, *The Journal of Chemical Physics* **1999,** 110 (13), 6158-6170.
39. Dovesi, R.; Erba, A.; Orlando, R.; Zicovich-Wilson, C. M.; Civalleri, B.; Maschio, L.; Rérat, M.; Casassa, S.; Baima, J.; Salustro, S.; Kirtman, B., Quantum-mechanical condensed matter simulations with CRYSTAL, *Wiley Interdisciplinary Reviews: Computational Molecular Science* **2018,** 0 (0), e1360.
40. Kröger, F. A.; Vink, H. J. In *Solid State Physics*, Seitz, F., Turnbull, D., Eds. Academic Press: 1956; Vol. 3, pp 307-435.
41. Monkhorst, H. J.; Pack, J. D., Special points for Brillouin-zone integrations, *Physical Review B* **1976,** 13 (12), 5188-5192.
42. Dai, J.-Q.; Zhu, J.-H.; Xu, J.-W., First-principles investigation of platinum monolayer adsorption on the $BiFeO_3$ (0001) polar surfaces, *Applied Surface Science* **2018,** 428, 964-971.
43. Ribeiro, R. A. P.; Andrés, J.; Longo, E.; Lazaro, S. R., Magnetism and multiferroic properties at $MnTiO_3$ surfaces: A DFT study, *Applied Surface Science* **2018,** 452, 463-472.
44. Tian, X.; Wang, T.; Fan, L.; Wang, Y.; Lu, H.; Mu, Y., A DFT based method for calculating the surface energies of asymmetric MoP facets, *Applied Surface Science* **2018,** 427, 357-362.
45. Viñes, F.; Konstantatos, G.; Illas, F., Matildite Contact with Media: First-Principles Study of $AgBiS_2$ Surfaces and Nanoparticle Morphology, *The Journal of Physical Chemistry B* **2018,** 122 (2), 521-526.
46. Andrés, J.; Gracia, L.; Gouveia, A. F.; Ferrer, M. M.; Longo, E., Effects of surface stability on the morphological transformation of metals and metal oxides as investigated by first-principles calculations, *Nanotechnology* **2015,** 26 (40), 405703.
47. Ferrer, M. M.; Gouveia, A. F.; Gracia, L.; Longo, E.; Andrés, J., A 3D platform for the morphology modulation of materials: first principles calculations on the thermodynamic stability and surface structure of metal oxides: Co_3O_4,α-Fe_2O_3, and In_2O_3, *Modelling and Simulation in Materials Science and Engineering* **2016,** 24 (2), 025007.
48. Oliveira, M. C.; Gracia, L.; de Assis, M.; Rosa, I. L. V.; do Carmo Gurgel, M. F.; Longo, E.; Andrés, J., Mechanism of photoluminescence in intrinsically disordered $CaZrO_3$ crystals: First principles modeling of the excited electronic states, *Journal of Alloys and Compounds* **2017,** 722, 981-995.

49. Ribeiro, R. A. P.; Lacerda, L. H. S.; Longo, E.; Andrés, J.; de Lazaro, S. R., Towards enhancing the magnetic properties by morphology control of $ATiO_3$(A = Mn, Fe, Ni) multiferroic materials, *Journal of Magnetism and Magnetic Materials* **2019,** 475, 544-549.
50. Ribeiro, R. A. P.; de Lazaro, S. R.; Gracia, L.; Longo, E.; Andrés, J., Theoretical approach for determining the relation between the morphology and surface magnetism of Co_3O_4, *Journal of Magnetism and Magnetic Materials* **2018,** 453, 262-267.
51. Gracia, L.; Andrés, J.; Longo, V. M.; Varela, J. A.; Longo, E., A theoretical study on the photoluminescence of $SrTiO_3$, *Chemical Physics Letters* **2010,** 493 (1-3), 141-146.
52. Teixeira, M. M.; de Oliveira, R. C.; Oliveira, M. C.; Pontes Ribeiro, R. A.; de Lazaro, S. R.; Li, M. S.; Chiquito, A. J.; Gracia, L.; Andrés, J.; Longo, E., Computational Chemistry Meets Experiments for Explaining the Geometry, Electronic Structure, and Optical Properties of $Ca_{10}V_6O_{25}$, *Inorganic Chemistry* **2018,** 57 (24), 15489-15499.
53. Oliveira, M. C.; Andrés, J.; Gracia, L.; de Oliveira, M. S. M. P.; Mercury, J. M. R.; Longo, E.; Nogueira, I. C., Geometry, electronic structure, morphology, and photoluminescence emissions of BaW1-xMoxO4 (x = 0, 0.25, 0.50, 0.75, and 1) solid solutions: Theory and experiment in concert, *Applied Surface Science* **2019,** 463, 907-917.
54. Norby, P.; Dinnebier, R.; Fitch, A. N., Decomposition of Silver Carbonate; the Crystal Structure of Two High-Temperature Modifications of Ag_2CO_3, *Inorganic Chemistry* **2002,** 41 (14), 3628-3637.
55. Jiang, W.; Wang, X.; Wu, Z.; Yue, X.; Yuan, S.; Lu, H.; Liang, B., Silver Oxide as Superb and Stable Photocatalyst under Visible and Near-Infrared Light Irradiation and Its Photocatalytic Mechanism, *Industrial & Engineering Chemistry Research* **2015,** 54 (3), 832-841.
56. Jiang, W.; Wu, Z.; Zhu, Y.; Tian, W.; Liang, B., Systematic research on Ag_2X (X=O, S, Se, Te) as visible and near-infrared light driven photocatalysts and effects of their electronic structures, *Applied Surface Science* **2018,** 427, 1202-1216.
57. Li, M.; Dai, Y.; Ma, X.; Jing, T.; Huang, B., Insights into the effect of inner polarization and multiple Ag-O units on high-efficient Ag-based photocatalyst, *Applied Catalysis B: Environmental* **2017,** 205, 211-218.
58. Yin, Y.; Chen, G.; Duan, X.; Ye, H.; Jin, W.; Zhu, Y.; Wu, Y., First-principles study on native point defects of cubic cuprite Ag_2O, *Journal of Applied Physics* **2016,** 120 (21), 215707.
59. Pereiro, M.; Baldomir, D.; Arias, J. E., Unexpected magnetism of small silver clusters, *Physical Review A* **2007,** 75 (6), 063204.
60. Luo, W.; Pennycook, S. J.; Pantelides, S. T., s-Electron Ferromagnetism in Gold and Silver Nanoclusters, *Nano Letters* **2007,** 7 (10), 3134-3137.
61. Marenco, A. J.; Pedersen, D. B.; Trudel, S., On the origin of the ferromagnetic signature in silver nanoparticles and thin films, *Journal of Materials Chemistry C* **2017,** 5 (20), 4899-4908.
62. Sargolzaei, M.; Lotfizadeh, N., Spin and orbital magnetism of a single 3d transition-metal atom doped into icosahedral coinage-metal clusters X_{12} (X = Cu, Ag, Au), *Physical Review B* **2011,** 83 (15), 155404.
63. Singh, G.; Chan, H.; Baskin, A.; Gelman, E.; Repnin, N.; Král, P.; Klajn, R., Self-assembly of magnetite nanocubes into helical superstructures, *Science* **2014,** 345 (6201), 1149.

64. Lazaro, S. R. d.; Ribeiro, R. A. P.; Lacerda, L. H. d. S. In *Titanium Dioxide*, Janus, M., Ed. Intechopen: 2017.
65. Le Bahers, T.; Rérat, M.; Sautet, P., Semiconductors Used in Photovoltaic and Photocatalytic Devices: Assessing Fundamental Properties from DFT, *The Journal of Physical Chemistry C* **2014,** 118 (12), 5997-6008.
66. Nørskov, J. K.; Bligaard, T.; Rossmeisl, J.; Christensen, C. H., Towards the computational design of solid catalysts, *Nature Chemistry* **2009,** 1, 37.
67. Hautier, G.; Miglio, A.; Waroquiers, D.; Rignanese, G.-M.; Gonze, X., How Does Chemistry Influence Electron Effective Mass in Oxides? A High-Throughput Computational Analysis, *Chemistry of Materials* **2014,** 26 (19), 5447-5458.
68. Luttrell, T.; Halpegamage, S.; Tao, J.; Kramer, A.; Sutter, E.; Batzill, M., Why is anatase a better photocatalyst than rutile? - Model studies on epitaxial TiO_2 films, *Scientific Reports* **2014,** 4, 4043.
69. Liao, P.; Carter, E. A., New concepts and modeling strategies to design and evaluate photo-electro-catalysts based on transition metal oxides, *Chemical Society Reviews* **2013,** 42 (6), 2401-2422.
70. Zhang, J.; Zhou, P.; Liu, J.; Yu, J., New understanding of the difference of photocatalytic activity among anatase, rutile and brookite TiO_2, *Physical Chemistry Chemical Physics* **2014,** 16 (38), 20382-20386.
71. Soares, G. B.; Ribeiro, R. A. P.; de Lazaro, S. R.; Ribeiro, C., Photoelectrochemical and theoretical investigation of the photocatalytic activity of TiO_2:N, *RSC Advances* **2016,** 6 (92), 89687-89698.
72. Xiangchao, M.; Ying, D.; Meng, G.; Baibiao, H., The Role of Effective Mass of Carrier in the Photocatalytic Behavior of Silver Halide-Based Ag@AgX (X=Cl, Br, I): A Theoretical Study, *ChemPhysChem* **2012,** 13 (9), 2304-2309.
73. Fishman, M.; Zhuang, H. L.; Mathew, K.; Dirschka, W.; Hennig, R. G., Accuracy of exchange-correlation functionals and effect of solvation on the surface energy of copper, *Physical Review B* **2013,** 87 (24), 245402.
74. Zhang, N.; Chen, C.; Mei, Z.; Liu, X.; Qu, X.; Li, Y.; Li, S.; Qi, W.; Zhang, Y.; Ye, J.; Roy, V. A. L.; Ma, R., Monoclinic Tungsten Oxide with {100} Facet Orientation and Tuned Electronic Band Structure for Enhanced Photocatalytic Oxidations, *ACS Applied Materials & Interfaces* **2016,** 8 (16), 10367-10374.
75. Scanlon, M. D.; Peljo, P.; Méndez, M. A.; Smirnov, E.; Girault, H. H., Charging and discharging at the nanoscale: Fermi level equilibration of metallic nanoparticles, *Chemical Science* **2015,** 6 (5), 2705-2720.
76. Rajabi, A.; Ghazali, M. J.; Mahmoudi, E.; Baghdadi, A. H.; Mohammad, A. W.; Mustafah, N. M.; Ohnmar, H.; Naicker, A. S., Characterization, and Antibacterial Activity of Ag_2O-Loaded Polyethylene Terephthalate Fabric via Ultrasonic Method, *Nanomaterials* **2019,** 9.
77. Tan, C.-S.; Chen, Y.-J.; Hsia, C.-F.; Huang, M. H., Facet-Dependent Electrical Conductivity Properties of Silver Oxide Crystals, *Chemistry – An Asian Journal* **2017,** 12 (3), 293-297.
78. Barmparis, G. D.; Lodziana, Z.; Lopez, N.; Remediakis, I. N., Nanoparticle shapes by using Wulff constructions and first-principles calculations, *Beilstein Journal of Nanotechnology* **2015,** 6, 361-368.
79. Pearson, R. G. In *Chemical Hardness*, Wiley: Weinheim 1997; pp 1-27.

80. Gouveia, A. F.; Assis, M.; Cavalcante, L. S.; Gracia, L.; Longo, E.; Juan, A., Reading at exposed surfaces: theoretical insights into photocatalytic activity of $ZnWO_4$, *Frontier Research Today* **2018,** 1, 1005.
81. Huang, C.-K.; Wu, T.; Huang, C.-W.; Lai, C.-Y.; Wu, M.-Y.; Lin, Y.-W., Enhanced photocatalytic performance of $BiVO_4$ in aqueous $AgNO_3$ solution under visible light irradiation, *Applied Surface Science* **2017**, 10-19.
82. Wu, S.-Z.; Li, K.; Zhang, W.-D., On the heterostructured photocatalysts Ag_3VO_4/g-C_3N_4 with enhanced visible light photocatalytic activity, *Applied Surface Science* **2015,** 324, 324-331.
83. Brunet, L.; Lyon, D. Y.; Hotze, E. M.; Alvarez, P. J. J.; Wiesner, M. R., Comparative Photoactivity and Antibacterial Properties of C_{60} Fullerenes and Titanium Dioxide Nanoparticles, *Environmental Science & Technology* **2009,** 43 (12), 4355-4360.
84. Xu, L.; Wei, Y.; Guo, W.; Guo, Y.; Guo, Y., One-pot solvothermal preparation and enhanced photocatalytic activity of metallic silver and graphene co-doped $BiVO_4$ ternary systems, *Applied Surface Science* **2015,** 332, 682-693.

Connecting the surface structure, morphology and photocatalytic activity of Ag_2O: An in depth and unified theoretical investigation

R. A. P. Ribeiro[1,*], Marisa C. Oliveira,[2] Maurício R. D. Bomio,[2] S. R. de Lazaro,[3] J. Andrés[4*], E. Longo[1*]

[1] *CDMF-UFSCar, Universidade Federal de São Carlos, PO Box 676, 13565–905 São Carlos, SP, Brazil*

[2] *LSQM- Laboratório de Síntese Química de Materiais, DEMat, Universidade Federal do Rio Grande do Norte - UFRN, P.O. Box 1524, 59078-970 Natal, RN, Brazil*

[3] *Department of Chemistry, State University of Ponta Grossa, Av. General Carlos Cavalcanti, 4748, 84030-900, Ponta Grossa, PR, Brazil*

[4] *Department of Physical and Analytical Chemistry, University Jaume I (UJI), Castelló 12071, Spain*

**corresponding authors; Email address: ribeiroapr@gmail.com; elson.liec@gmail.com; andres@qfa.uji.es*

Figures

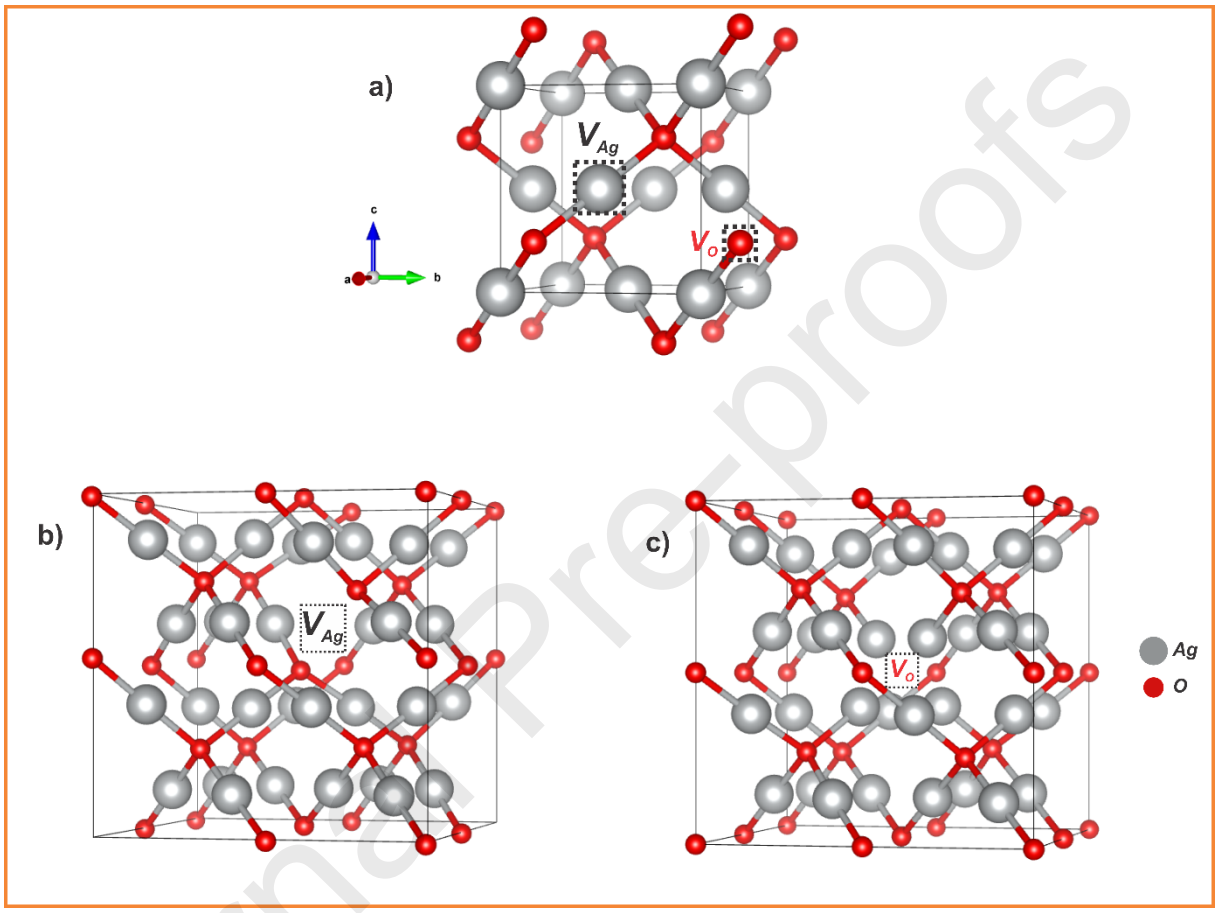

Figure 1. A schematic 3D representation of the structures for (a) Ag_2O and defective supercells (2 x 2 x 2) for neutral and charged (b) V_{Ag} and (c) V_O vacancies.

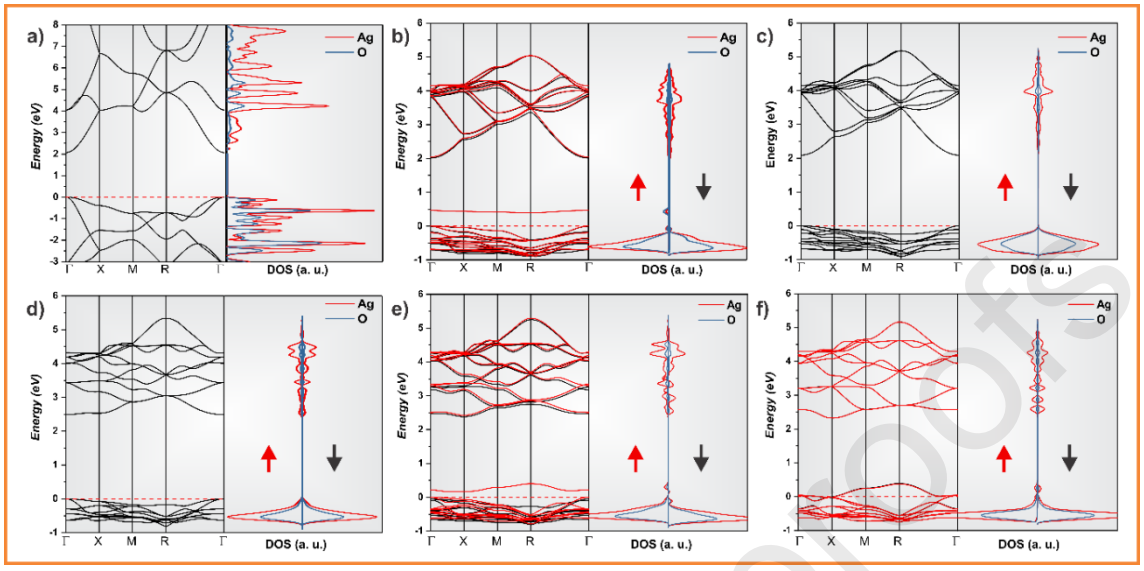

Figure 2. Density of state profiles and band structure for (a) pristine Ag_2O model and defective supercell containing (b) V_{Ag}^{x}, (c) V'_{Ag}, (d) V_{O}^{x}, (e) $V_{O}^{\bullet}$ and (f) $V_{O}^{\bullet\bullet}$ centers. In all cases the Fermi level was set to zero. The black and red arrows correspond to the spin-up and spin-down orientations, following the black and red dispersion curves on the band structure.

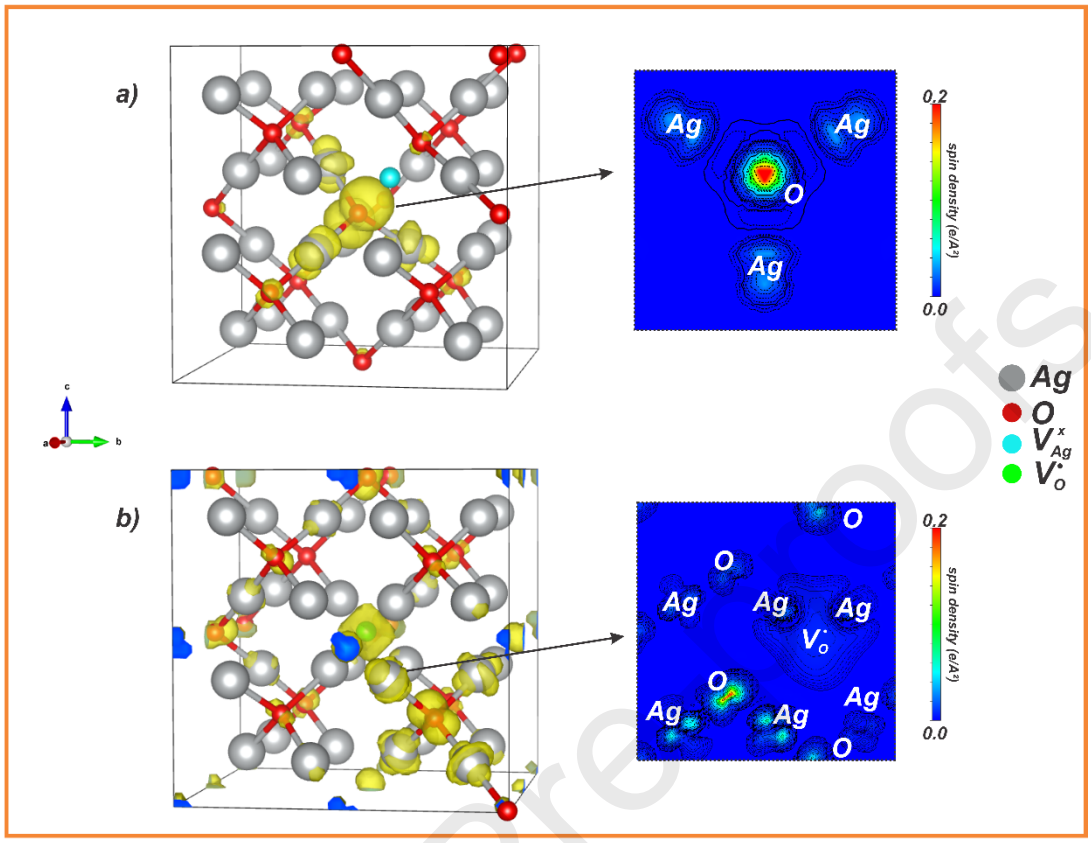

Figure 3. Spin density isosurfaces (0.002 e/A³) for Ag_2O containing (a) V_{Ag}^{x} and (b) $V_O^{\bullet}$ centers. The yellow density correspond to the unpaired electron associated with the hole generated from V_{Ag} In the right panel a 2D plot of the spin density containing the atoms involved in the stabilization of remaining electron.

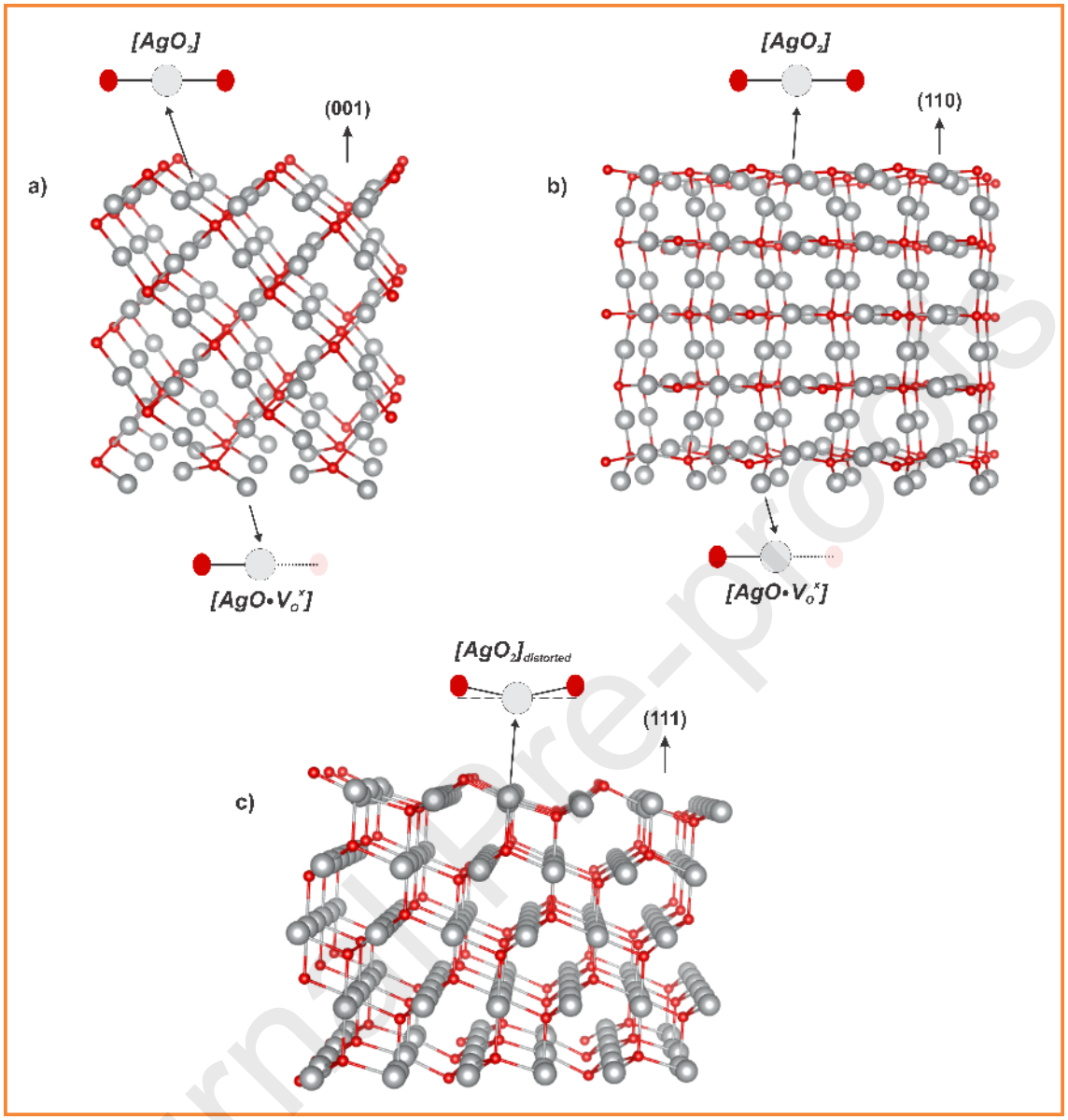

Figure 4. Representation of optimized (100), (110) and (111) surfaces of Ag_2O.

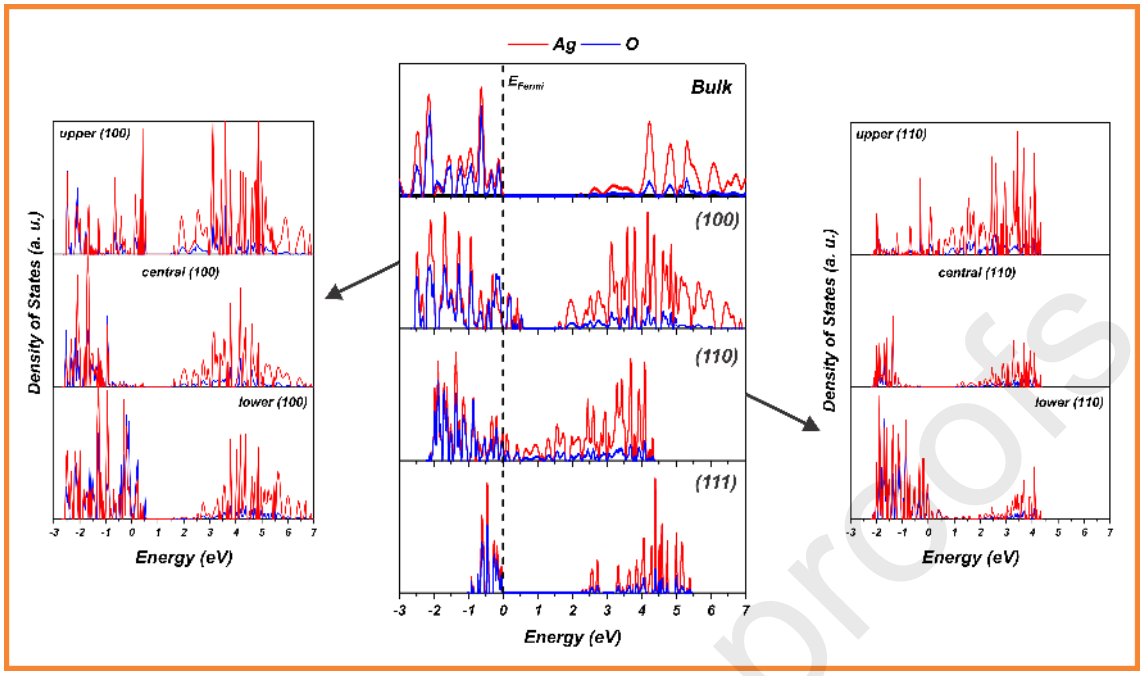

Figure 5. Density of states for Ag_2O bulk and (100), (110) and (111) surfaces. In the left and right panels the upper, central and lower surface contributions for both polar (100) and (110) surfaces is presented. For non-polar (111) surface the upper and lower contribution is the same. In all cases the Fermi level was set to zero.

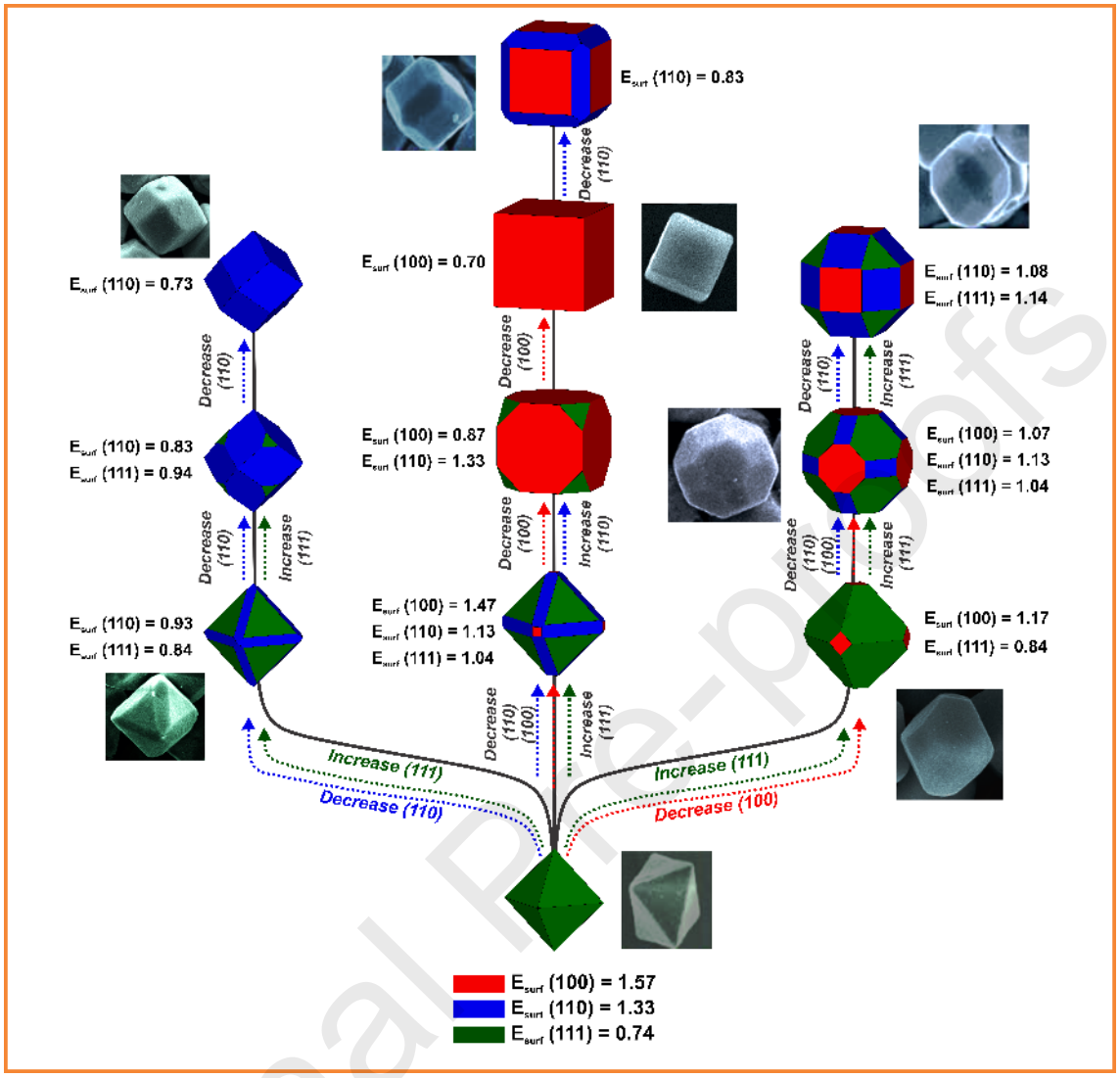

Figure 6. Morphological map proposed for Ag_2O using (100), (110) and (111) surface energies (J/m²) calculated at DFT/B3LYP level of theory. Experimental morphologies were Reproduced from Ref. [20] with permission from The Royal Society of Chemistry. Reprinted with permission from Y-J. Chen, Y-W. Chiang, M. H. Huang, Synthesis of Diverse Ag_2O Crystals and Their Facet-Dependent Photocatalytic Activity Examination. Copyright 2016 American Chemical Society from Ref [22]. All experimental images were obtained using Scanning Electron Microscopy (SEM).

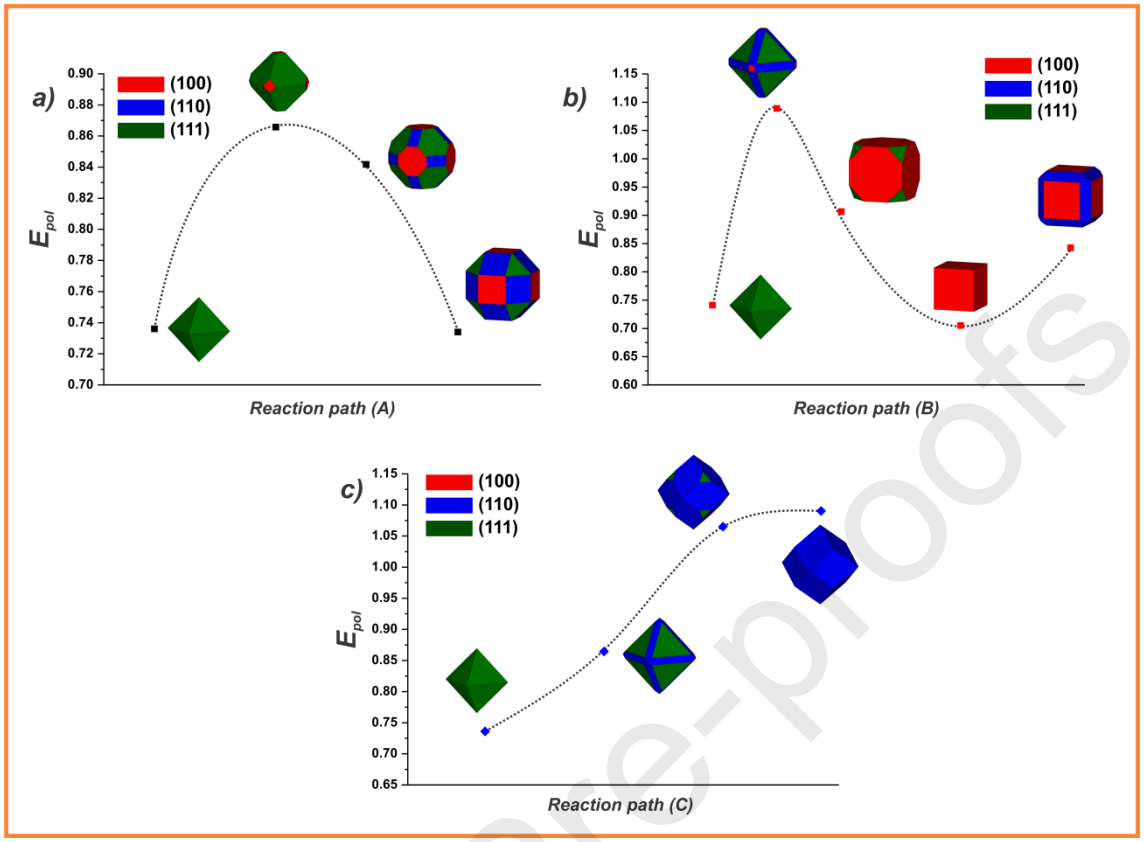

Figure 7. Schematic illustration of the energy profile for different Ag_2O morphologies. The polyhedron energy, E_{pol}, is plotted *versus* the corresponding reaction path. Intermediate morphologies were obtained by decreasing/increasing of E_{surf} values involved in the process.

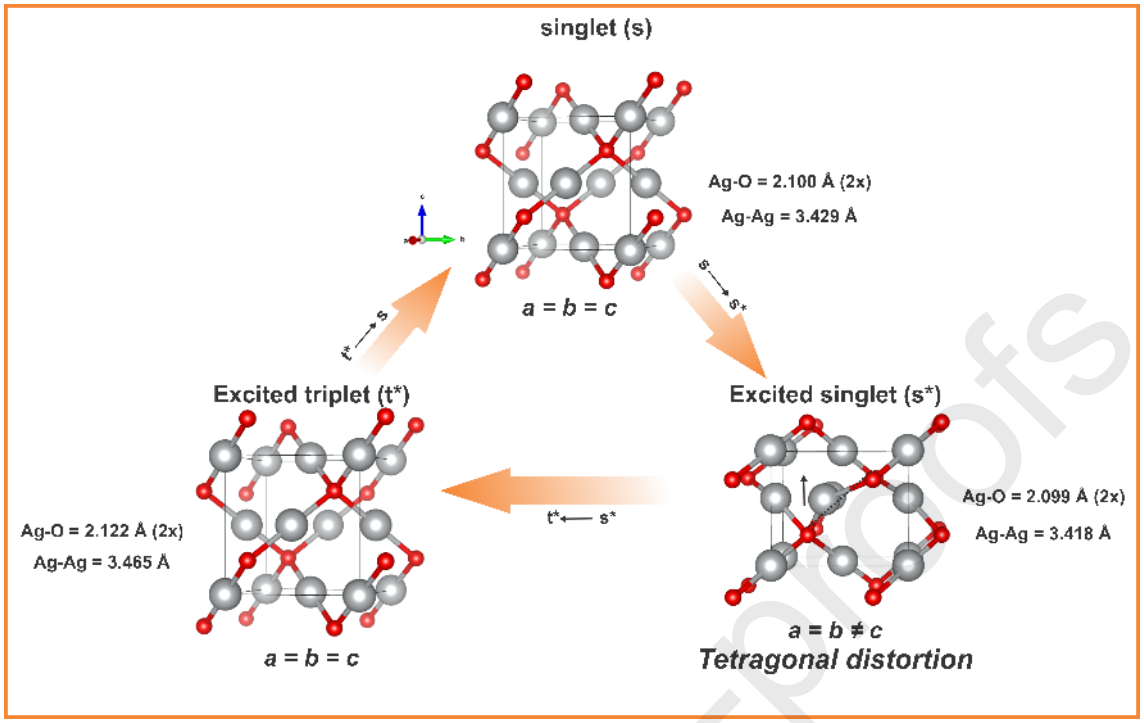

Figure 8. Schematic representation of the main changes associated with the transformation of fundamental singlet (s) state to excited singlet (s*) and triplet (t*) electronic states.

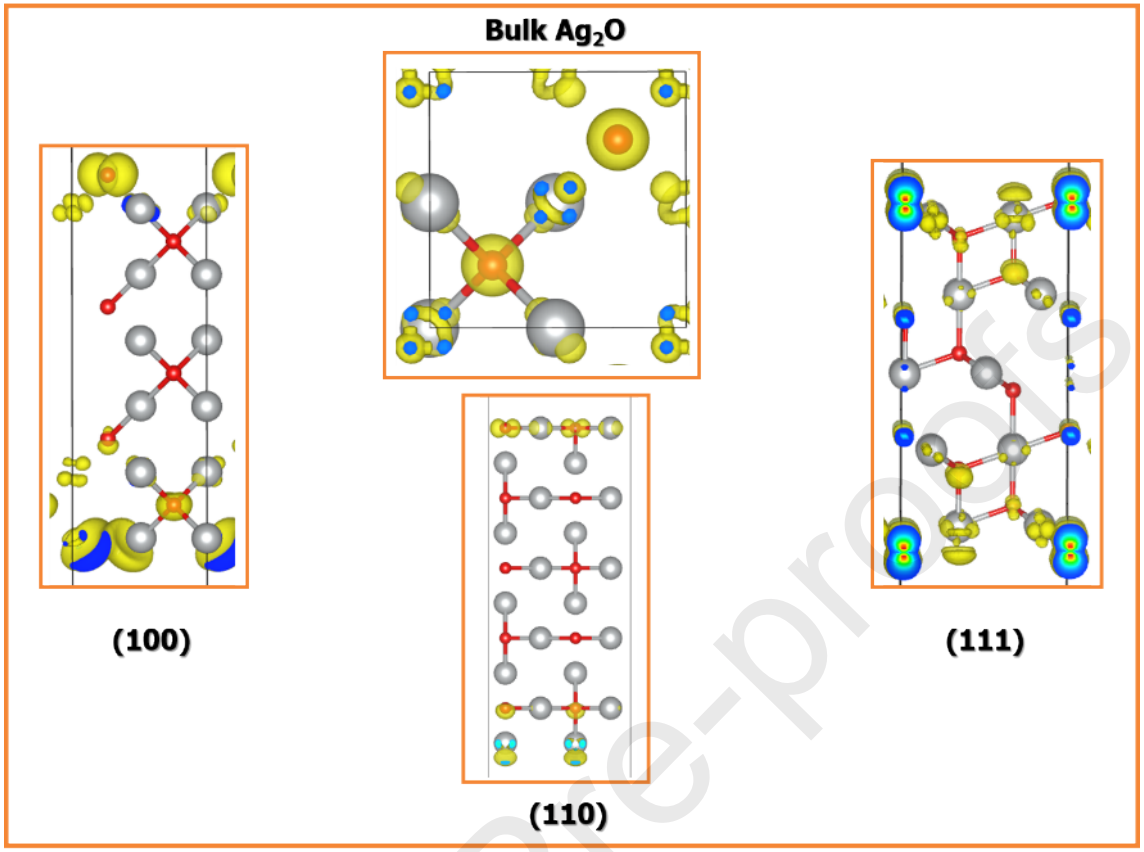

Figure 9. Spin density isosurface (0.001 e/Å^3) for Ag_2O bulk and (100), (110) and (111) surfaces at the excited triplet (t*) states. In all cases, yellow and blue isosurfaces correspond to positive and negative spin densities.

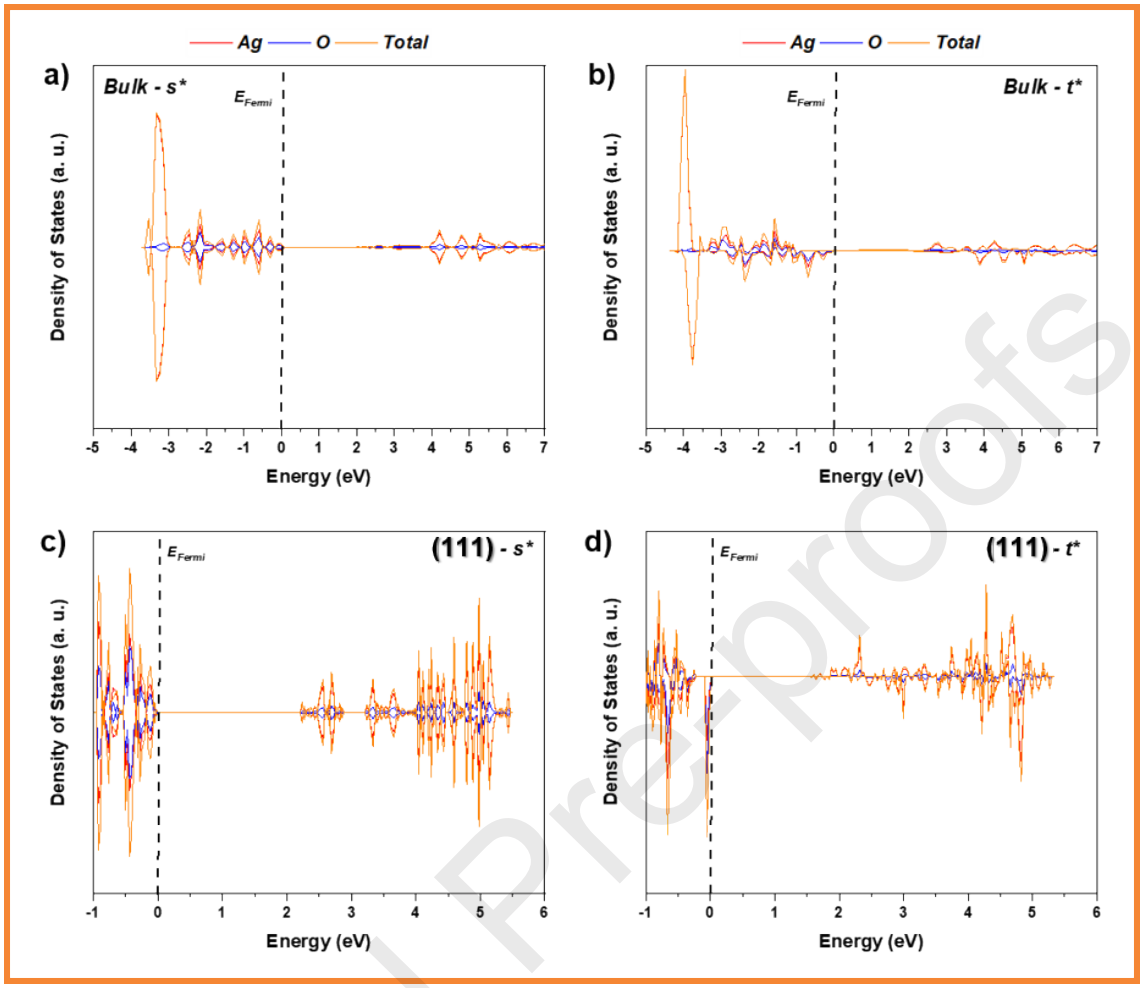

Figure 10. Density of states for Ag_2O bulk and (111) surface at excited (a, c) singlet (s*) and (b, d) triplet (t*) electronic states.

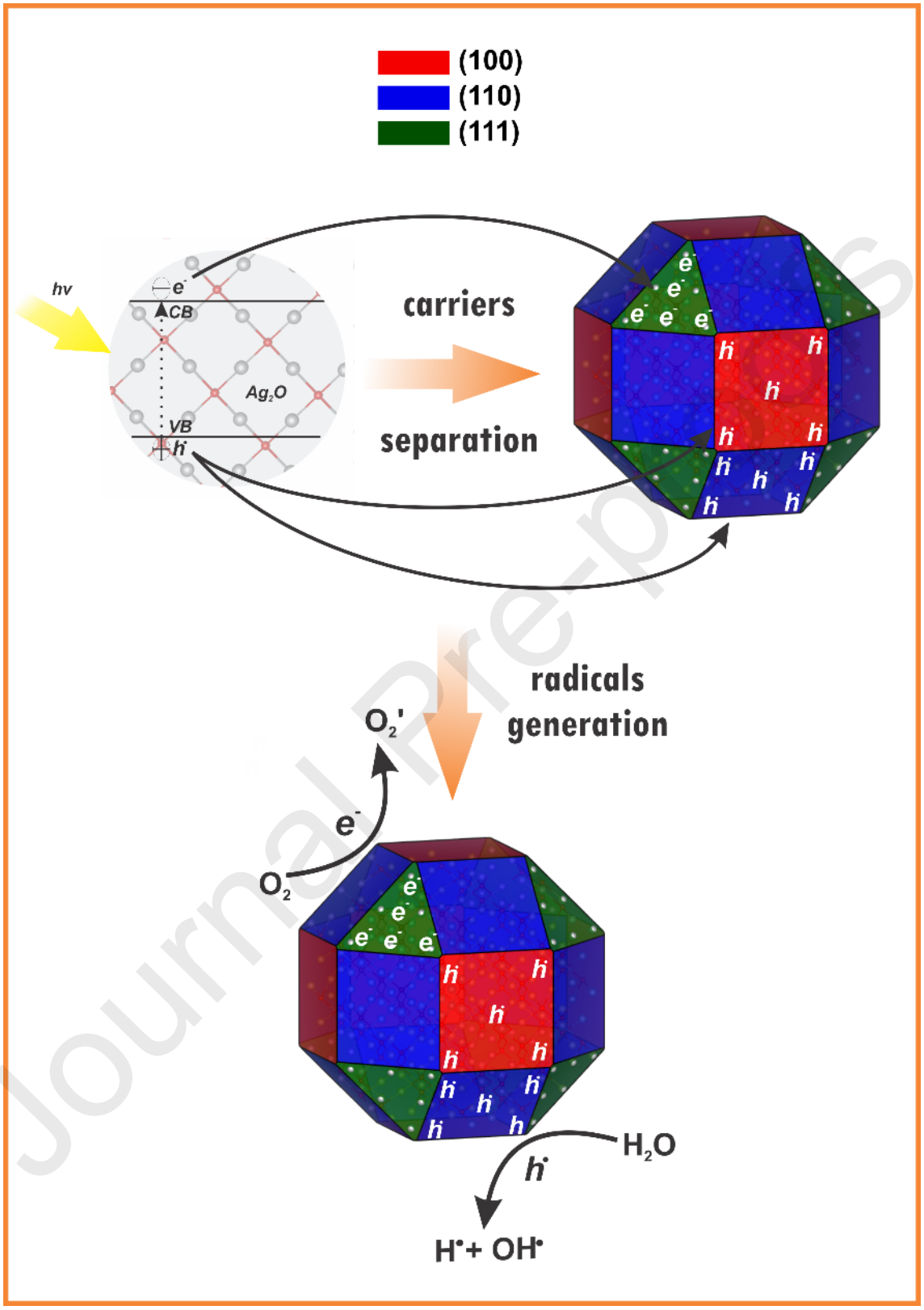

Figure 11. Schematic representation of the photocatalytic mechanism in shape-oriented Ag_2O materials.

Supporting Information

In order to confirm the viability of the proposed method reported in this manuscript, we compare the calculate E_{surf} value for (100) surface obtained with equations 1-3 with the relaxed cleavage energy ($E_{cleav}^{relax}(Z^+|Z^-)$obtained by symmetric and non-stoichiometric surfaces as proposed by Heifets *et al*.[1] In this case, two symmetric and non-stoichiometric were considered to represent the Z^+ (O-Ag_2-) and Z^- (Ag_2-O-) terminations and the $E_{cleav}^{relax}(Z^+|Z^-)$ was calculated following the equation:

$$\boldsymbol{E_{cleav}^{relax}(Z^+|Z^-) = \frac{\left(E_{slab}^{rlx}[Z^+] + E_{slab}^{rlx}[Z^-] - nE_{bulk}\right)}{4A}} \quad (1)$$

In this case, the calculated value of E_{surf} reported with the method proposed here (Eq. 1-3) was 1.58 J/m² in closer agreement with the result (1.60 J/m²) obtained following the Heifets *et al.* methodology. [1] This fact confirms that the employed method is capable to represent correctly the materials surface energetics.

1. E. Heifets, R. I. Eglitis, E. A. Kotomin, J. Maier and G. Borstel, *Surface Science*, 2002, **513**, 211-220.

Table S1. Surface area composition, E_{surf} and E_{pol} for the different proposed morphologies.

	(100)		(110)		(111)		E_{pol}
	E_{surf}	%	E_{surf}	%	E_{surf}	%	
Ideal	1.575	0.0	1.334	0.0	0.736	100.0	0.736
1.0	1.575	0.0	0.934	30.3	0.836	69.7	0.866
1.1	1.575	0.0	0.834	92.4	0.936	7.6	0.842
1.2	1.575	0.0	0.734	100.0	0.936	0.0	0.734
2.0	1.475	3.2	1.134	34.5	1.036	62.3	1.084
2.1	0.875	92.7	1.334	0.0	1.236	7.3	0.901
2.2	0.700	100.0	1.334	0.0	1.236	0.0	0.700
2.3	0.700	73.4	0.834	0.0	1.236	26.6	0.843
3.0	1.175	8.4	1.334	0.0	0.836	91.6	0.865
3.1	1.075	40.8	1.134	13.5	1.036	45.7	1.065
3.2	1.075	42.4	1.084	38.4	1.136	19.2	1.090

Table S2. Atomic charges |e| for Ag and O atoms along the (100), (110) and (111) surfaces of Ag_2O for fundamental singlet (s), excited singlet (s*) and excited triplet (t*) states.

Surfaces	Terminations	Atomic Charges	
		Ag	O
Singlet (s)			
(100)	Z^+	0.539	-0.702
	Z^-	0.248	-0.805
(110)	Z^+	0.527	-0.787
	Z^-	0.322	-0.795
(111)	-	0.205	-0.834
Excited Singlet (s*)			
(100)	Z^+	0.536	-0.702
	Z^-	0.249	-0.804
(110)	Z^+	0.531	-0.789
	Z^-	0.323	-0.798
(111)	-	0.206	-0.832
Excited Triplet (t*)			
(100)	Z^+	0.678	-0.525
	Z^-	0.227	-0.830
(110)	Z^+	0.559	-0.788
	Z^-	0.227	-0.824
(111)	-	0.142	-0.762

Table S3. Raman modes calculated at B3LYP level of theory for fundamental singlet (s), excited singlet (s*) and excited triplet (t*) states. R, B, S correspond to rotational, bending and stretching.

Singlet (s)		
Frequency (cm^{-1})	Symmetry Representation	Characterization
438.44	F2g	B
Excited singlet (s*)		
Frequency (cm^{-1})	Symmetry Representation	Characterization
55.82	B"	R
57.60	B"	R
57.65	A'	R
80.09	B"	R
80.28	A'	R
89.82	A'	R
89.97	A'	R
90.17	B"	R
254.74	A'	S
431.17	A'	B
441.21	A'	S
441.70	B"	B
533.35	A'	B
540.02	A'	S
540.68	B"	S
Excited triplet (t*)		

Frequency (cm^{-1})	Symmetry Representation	Characterization
420.19	F2g	B

Table S4. Cleavage energy convergence test.

Surface	Thickness (Å)	E_{cleav}^{unrlx} (J/m^2)
(100)	3.32	1.75
	8.48	1.99
	13.5	2.01
(110)	1.70	1.14
	5.14	1.46
	8.58	1.51
	12.02	1.55
	15.5	1.56
(111)	1.40	0.74
	4.20	0.79
	6.98	0.76
	9.76	0.77
	13.8	0.78

Declaration of interests

☒ The authors declare that they have no known competing financial interests or personal relationships that could have appeared to influence the work reported in this paper.

☐The authors declare the following financial interests/personal relationships which may be considered as potential competing interests:

Connecting the surface structure, morphology and photocatalytic activity of Ag_2O: An in depth and unified theoretical investigation

R. A. P. Ribeiro[1,*], Marisa C. Oliveira,[2] Maurício R. D. Bomio,[2] S. R. de Lazaro,[3] J. Andrés[4*], E. Longo[1*]

[1] *CDMF-UFSCar, Universidade Federal de São Carlos, PO Box 676, 13565–905 São Carlos, SP, Brazil*

[2] *LSQM- Laboratório de Síntese Química de Materiais, DEMat, Universidade Federal do Rio Grande do Norte - UFRN, P.O. Box 1524, 59078-970 Natal, RN, Brazil*

[3] *Department of Chemistry, State University of Ponta Grossa, Av. General Carlos Cavalcanti, 4748, 84030-900, Ponta Grossa, PR, Brazil*

[4] *Department of Physical and Analytical Chemistry, University Jaume I (UJI), Castelló 12071, Spain*

**corresponding authors; Email address: ribeiroapr@gmail.com; elson.liec@gmail.com; andres@qfa.uji.es*

Graphical Abstract

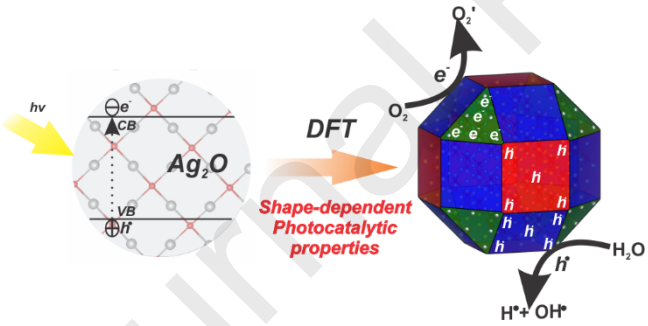

Identifying the most active surfaces and the corresponding electronic structures associated with the surface redox centers is essential for the rational design of Ag_2O-based photocatalysts. In this study, comprehensive and systematic theoretical calculations revealed the connection between electronic structure and morphology responsible for the photo-induced mechanism in terms of composition, chemical environment, and electronic structure of the surface.

Connecting the surface structure, morphology and photocatalytic activity of Ag_2O: An in depth and unified theoretical investigation

R. A. P. Ribeiro[1,*], Marisa C. Oliveira,[2] Maurício R. D. Bomio,[2] S. R. de Lazaro,[3] J. Andrés[4*], E. Longo[1*]

[1] *CDMF-UFSCar, Universidade Federal de São Carlos, PO Box 676, 13565–905 São Carlos, SP, Brazil*

[2] *LSQM- Laboratório de Síntese Química de Materiais, DEMat, Universidade Federal do Rio Grande do Norte - UFRN, P.O. Box 1524, 59078-970 Natal, RN, Brazil*

[3] *Department of Chemistry, State University of Ponta Grossa, Av. General Carlos Cavalcanti, 4748, 84030-900, Ponta Grossa, PR, Brazil*

[4] *Department of Physical and Analytical Chemistry, University Jaume I (UJI), Castelló 12071, Spain*

**corresponding authors; Email address: ribeiroapr@gmail.com; elson.liec@gmail.com; andres@qfa.uji.es*

Highlights

- A deep analysis of surface structure, native point defects and the photocatalytic activity of Ag_2O is presented;
- The shape-dependent photocatalytic properties were addressed to the charge carriers diffusion along (100), (110) and (111) surfaces;
- Fundamental and excited states were considered to describe the photo-induced mechanism;
- An in depth and unified theoretical protocol is proposed to design highly efficient photocatalysts